The EU Framework Programme for Research and Innovation H2020
Research and Innovation Action

Deliverable D3.3
Operator Interface Control, First Version of Control Station

Dissemination Level: Public

Project acronym:	CENTAURO
Project full title:	Robust Mobility and Dexterous Manipulation in Disaster Response by Fullbody Telepresence in a Centaur-like Robot
Grant agreement no.:	644839
Lead beneficiary:	SSSA – Scuola Superiore di Studi Universitari e di Perfezionamento Sant Anna
Authors:	Antonio Frisoli, Massimiliano Solazzi, Domenico Buongiorno, Daniele Leonardis, Massimiliano Gabardi, Mine Sarac, Michael Felsberg, Klas Nordberg
Work package:	WP3 – Operator Interfaces
Date of preparation:	2016-09-25
Type:	Report
Version number:	1.0

Document History

Version	Date	Author	Description
0.1	2017-09-25	Frisoli, Solazzi, Buongiorno, Leonardis, Gabardi, Sarac, Felsberg, Nordberg	First draft released
1.0			Submitted version

Executive Summary

This deliverable presents the first version of the operator control station to teleoperate the Centauro robot. The arms exoskeleton has been integrated with the wrist module and the hand exoskeleton, obtaining an innovative system to provide feedback on the whole upper limb. The operator can control robot navigation by two pedals with three degrees of freedom. Stereo visual feedback is provided by an Head Mounted Display. The bilateral teleoperation has been performed implementing a Position-Measured Force architecture with a Time Domain Passivity Approach-based controller and position-drift compensation to deal with communication delay.

Contents

1 Introduction

This Deliverable presents progress achieved in the development of the Centauro Control Station. In particular we present the development and final integration of the different modules composing the Control Station, comprising the different robotic exoskeleton modules worn at the arm, wrist and hand respectively, the immersive visualization module and the control pedals for controlling locomotion of the Centauro robot.

In the following paragraphs, progress in the development of the different modules for the final integration in the Control Station is presented. In particular, the Wrist Exoskeleton has been designed, implemented, characterized and controlled for the haptic rendering purposes of the Centauro teleoperation (Section 3). An experimental haptic rendering test in virtual reality with HMD has been conducted for validating the Wrist Exoskeleton. The Hand Exoskeleton module has been optimized in haptic rendering performance with a novel control strategy: this approach takes into account the underactuation of the finger mechanism of the Hand exoskeleton when rendering the stiffness of virtual or teleoperated grasped objects. Regarding the hand interface, the thumb exoskeleton has been designed, developed, experimentally validated and integrated on the hand exoskeleton. The developed mechanism achieves underactuation to 2 DoFs (1 DoF actuated) of the complex kinematics of the human thumb, supporting force feedback in grasping tasks and still preserving adaptation to different hand sizes (Section 4). The completed Arm, Wrist and Hand Exoskeletons have been thus integrated in a whole unit for teleoperation of the full arm movements and grasping functionalities of the Centauro. In Section 4.4, development of the software integration of the different modules and in particular of the hand modules within the ROS Framework and the GAZEBO simulation tool are shown. Hardware and software integration of the Control Pedals within the Control Station has been performed and presented in Section 6. The teleoperation functionalities of the Arm Exoskeleton have been experimented in a preliminary teleoperation setup with a second robotic arm and evaluated in Section 7. The processing of the visual information provided by robot cameras and RGBD sensors, consisting in real time transformation into a 3D scene for enhanced presentation to the remote operator through the HMD is presented in Section 8.

2 Control Station

The Control Station represents the physical control platform interfacing the remote operator with the Centauro robot. Such interface between the operator and the robot is bidirectional: the operator sends motor commands to the Centauro and at the same time perceives information sent by the robot, in terms of force and visual feedback.

The control modality of the complex motor functions of the Centauro robotic arms is designed to directly resemble real operator movements with the most natural and intuitive approach: by means of a full upper limb exoskeleton developed for the Control Station, the movements of the operator's upper limbs are transparently tracked by the robotic exoskeleton and sent to teleoperate movements of the Centauro's arms. At the same time, force feedback of the Centauro's arms interacting with the environment is sent back to the operator, by means of the exoskeleton active force feedback. With the additional integration of an immersive Head Mounted Display for real-time video streaming, the Control Station design aims to immerse the remote operator in the Centauro, enhancing complex and fine control capabilities by preserving the operator's natural motor and sensory modalities. Due to the grounded implementation of the complex exoskeletal modules of the Control Station, the control of the navigation functionalities of the Centauro robot are performed through a Pedals module developed and integrated

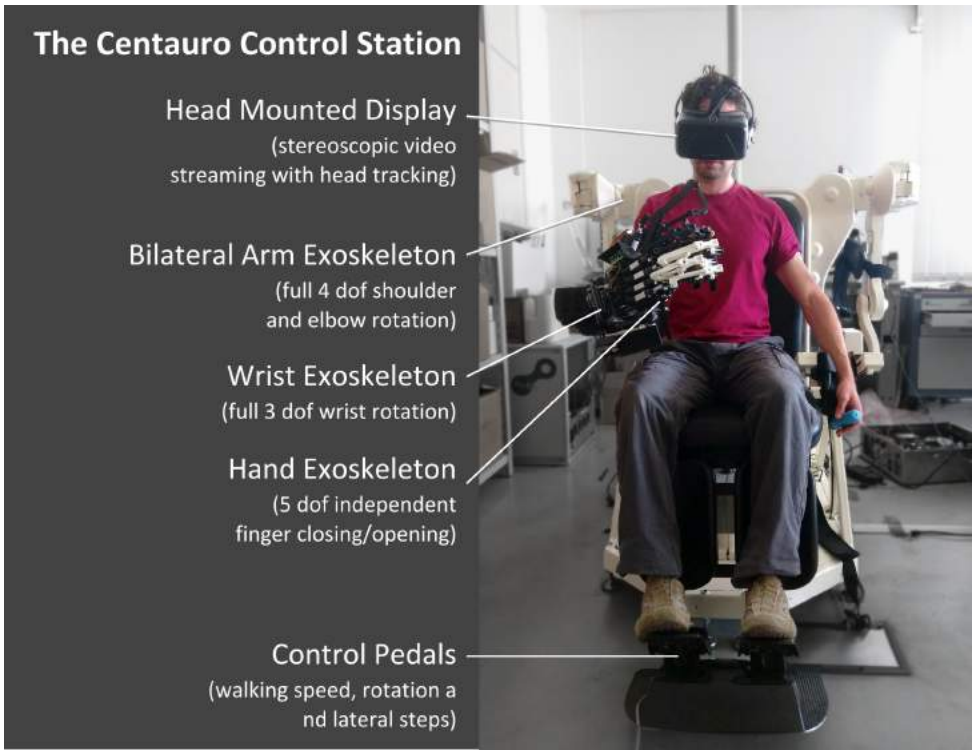

Figure 1

in the station.

Figure 1 shows the setup of the Centauro Control Station integrating the different modules in a whole control platform.

3 Wrist Exoskeleton Module

This section describe the wrist exoskeleton designed to provide kinesthetic feedback to the wrist user' joints teleoperation and virtual environment interaction purposes. The design process focused on the need to use the interface as the end-effector of a whole bimanual upper limb exoskeleton system, composed of two exoskeleton arms with four degrees of freedom (DoF), two wrist exoskeletons with three DoFs and two hand exoskeletons for all the fingers. The guideline of the design pointed to reach a trade-off between high transparency and low weight. In addition, both the compactness and mass distribution have played an important role in the design process due to the need to perform bimanual task and interaction.

The proposed device was designed adopting a tendon-cable transmission for all the three joints. A differential transmission solution has been adopted to actuate the flexion/extension and radial/ulnar deviation joints by using two-stage tendon transmissions. A first prototype has been build and characterized with several experimental tests showing its suitability for haptics and teleoperation. Finally, the wrist device has been integrated with both the arm and the hand exoskeleton to prove the requirement observance.

3.1 Introduction

In the last decade, the exploding need of both higher immersivity in physical virtual environment interaction and more advanced robotic interfaces has pushed the scientific community to

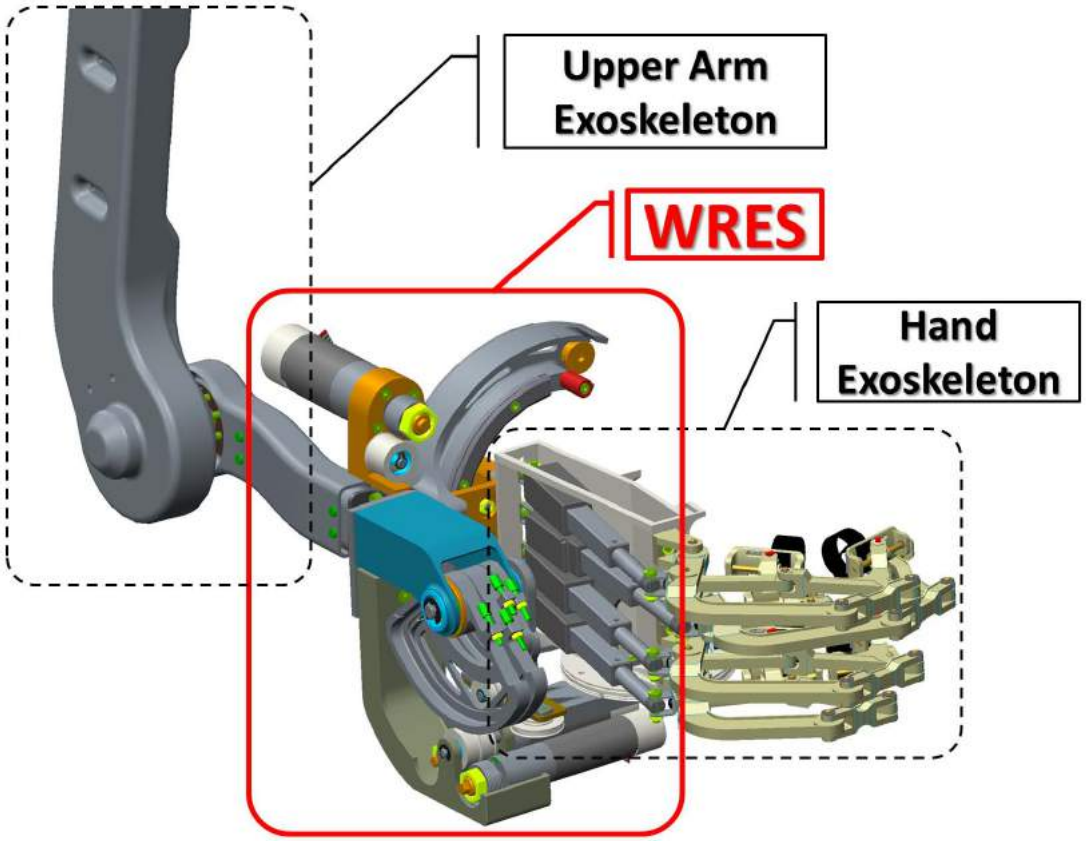

Figure 2: Basic configuration of the WRES interface with Hand exoskeleton interface, mounted on exoskeleton upper arm.

find new solutions for more complex robotic interfaces able to interact with the humans. Such a trend is explained by the growing interest in virtual environment physical interaction. In this scenario, exoskeletons represent an important component of telexistence cockpits [6]. An exoskeleton is a robotic device that can be worn on the user's body and represents the typical robotic system where the highest physical symbiosis with the human operator is achieved.

This section presents the design and experimental evaluation of a new three DoFs wrist exoskeleton, the WRES. The WRES is an active three-DoF wrist exoskeleton with a spherical serial kinematics and based on tendon transmissions.

The rationale behind this work is the design of a fully actuated bimanual upper limb exoskeleton system, as shown in figures 2 and 13. The whole system is devised to have two robotic arms exoskeleton with seven DoFs each (three for the shoulder articulation, one for the elbow joint and three for the wrist articulation) and two fully actuated hand exoskeletons. At SSSA premises both a bilateral arm exoskeleton (ALEx - Arm Light Exoskeleton) [40, 41] with the first 4 DoF (shoulder, elbow) and a new hand exoskeleton [45] have been already designed and evaluated. The new WRES wrist exoskeleton has been devised so to complete the fully actuated exoskeleton, and to this aim has to fulfill several requirements: (a) to be low-weight, in order to be mounted on the top of the ALEx exoskeleton; (b) to be able to accommodate the hand exoskeleton at its end-effector; (c) to be characterized by an optimal weight/actuation torques ratio; (d) to be compact with an optimal mass distribution allowing bimanual tasks, i.e. manipulation of small virtual or real objects (e.g. Kubric cube).

The WRES presented design (fig. 4) introduces a novel capstan-based tendon driven solution to actuate a differential transmission. To the authors' knowledge, for the first time a

differential transmission is designed with the encumbrance completely distributed on only one side. In the particular application of this paper, the differential transmission is used to actuate the flexion/extension and radial/ulnar deviation joints. Thanks to the optimal mass distribution, that is completely on the dorsal side of the human hand, the hand palm is free allowing bimanual task interaction with virtual and real objects. To ensure a high backdrivability, the first prono-supination joint is actuated with a tendon transmission, too. Since the rationale of the work is the development of a fully actuated bimanual upper limb exoskeleton, the design process took into account the mass distribution on the internal part of the forearm to avoid interferences between two worn wrist exoskeletons. The developed exoskeleton can be also mounted on a arm exoskeleton due to its high compactness and its low weight; in this particular work it has been mounted on the ALEx exoskeleton end-effector. Finally, to observe all the requirements, it can accommodate the PERCRO hand exoskeleton.

In the sections that follow, we present an overview of the state of the art, then the design and controller development, with details on the mechanical design and the actuation part first and the electronics, the low level control and friction compensation later. Finally, we present the results of the system identification and from testing experiments to evaluate its transparency and its capacity in haptic tasks.

3.2 Survey of Existing Literature

Several exoskeleton devices for upper limb interaction have been presented in the last years ([32]). Only few of them have more than four actuated DoFs necessary for the main upper limb articulations [38, 35, 25].

The CADEN 7 ([38]) is cable-actuated dexterous exoskeleton with seven actuated DoFs (four for the shoulder, one for the elbow and three for wrist). Both the ARMIN III ([35]) and HARMONY ([25]) have six actuated DoFs (four for the shoulder, one for the elbow and two for wrist). To the authors' knowledge a seven actuated DoFs upper limb exoskeleton with a fully actuated hand exoskeleton has not yet been presented. In addition to upper limb exoskeletons that might include some or all the wrist DoFs, several independent wrist robotic devices have

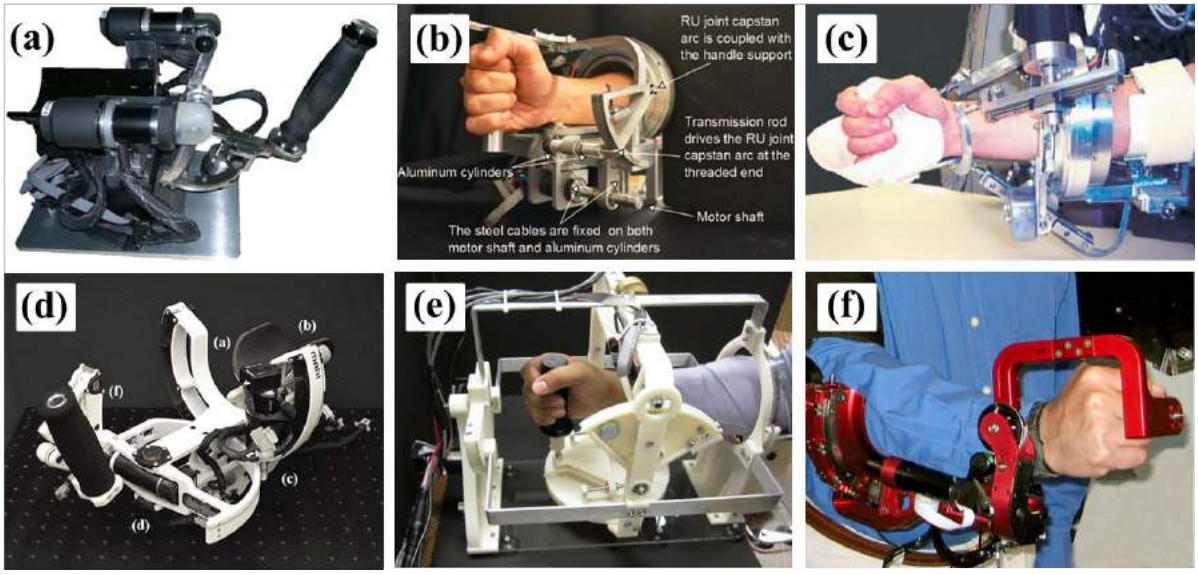

Figure 3: **Existing 3 DoFs wrist exoskeleton.** Figures (a), (b), (b), (d), (e) and (f) show the wrist exoskeletons presented in [8, 37, 20, 39, 33], and [38], respectively.

been presented so far ([8, 37, 20, 39, 33, 38]). As depicted in figure 3, the wrist exoskeleton solutions in literature are based on different approaches concerning the kinematics, the mechanics and the power transmission. The Wrist-Robot [8], developed at the Italian Institute of Technology and shown in figure 3a, has the high back-drivability of the 3 DoFs as main requirement. The mechanical solution is based on a serial kinematics actuated by gear motors; in particular the RU joint is actuated by two parallel coupled motors. The RiceWrist-S, reported in figure 3b, is cable-driven serial mechanism actuated by DC motors. Sergi, in [20], proposed a wrist robotic device (shown in figure 3c) based on a parallel structure and powered by linear series elastic actuators purposely designed for safety interaction. The high physical compliance guaranteed by this device comes at the expense of high encumbrance and difficulty to be don/doff. Like the RiceWrist-S, the OpenWrist, shown in figure 3d, employs a serial RRR mechanism for manipulation of the users wrist. Power is transmitted through capstan-cable drives. Several improvements and new features were implemented with respect to the precedent prototypes: polymer-ceramic coating, easiness in changing hand-side configuration, passive DoF to compensate axis misalignment, high performance and a simple don/doff procedure. The Wrist Gimbal, shown in figure 3e, is a three DoFs exoskeleton characterized by a high mechanical rigidity thanks to its parallel structure. The wrist module of the Caden 7 exoskeleton, reported in figure 3f, is an impedance-based wrist exoskeleton. It has three DoFs driven by a tendon-based transmission.

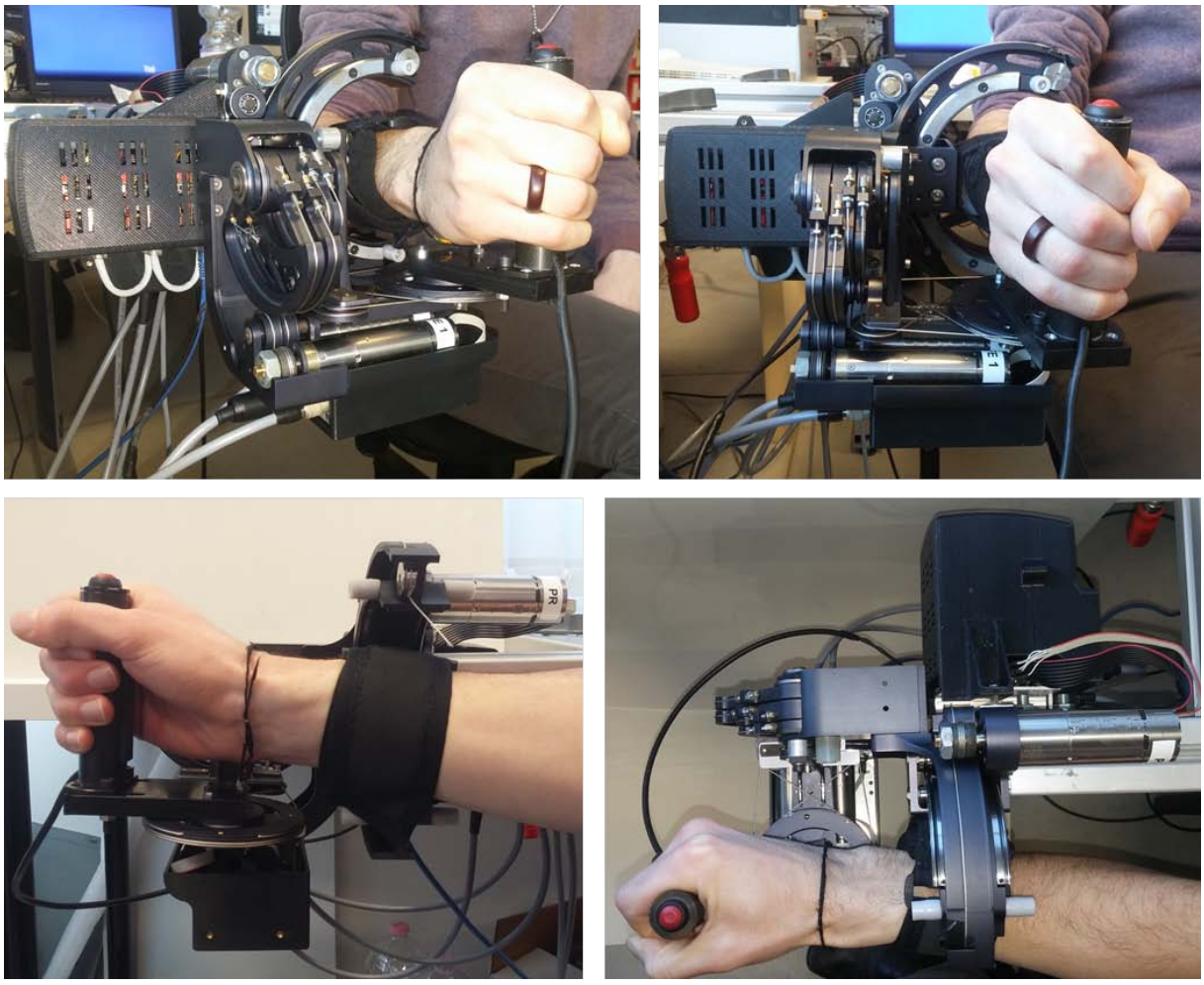

Figure 4: WRES device worn by a user.

All the devices described above are not suitable since they do not respect all the imposed requirements. Even though the solutions shown in figure 3a,b,c,d could accommodate the hand exoskeleton and could be mounted at the end-effector of an upper arm exoskeleton, the encumbrance of the fixed and moving parts doesn't allow their use in bimanual tasks. In fact, mounting any of the devices shown in figure 3a,b,c,d on two arm exoskeletons, some parts might interfere each other or with the opposite hand exoskeleton and human arm. Since these four exoskeletons have been thought as grounded devices, they present a significant mass distribution in the bottom part of the device. This feature would reduce a lot the workspace of a 7 DoFs system in the case of the user is a seated position since the wrist module can hit the legs. The solution reported in figure 3e would be hard to use is a not-grounded application. Finally, even if the solution shown in figure 3f is already a module of an upper limb exoskeleton and has a mass distribution that would allow a safe fine bimanual tasks, it cannot accommodate the hand exoskeleton due to the overall structure bulk.

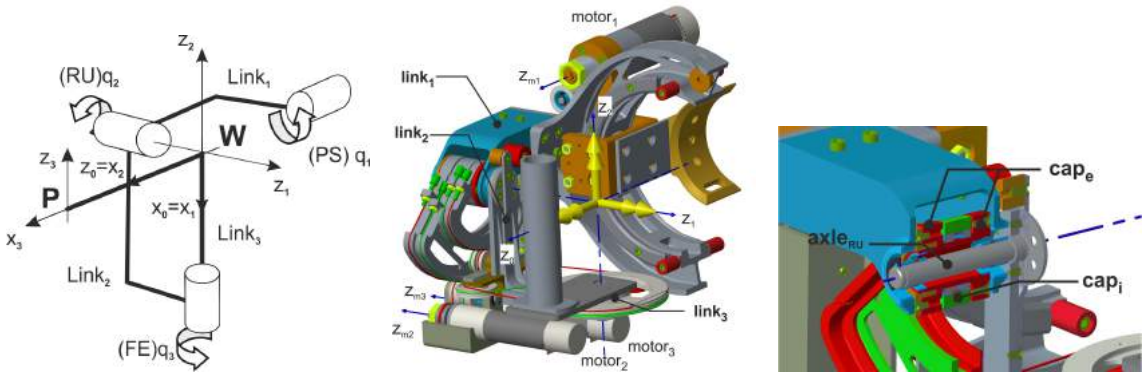

(a) (b) (c)

Figure 5: The schematic representation of wrist device kinematics is depicted in (a); the device's CAD model is shown in (b).
The section from the CAD model, in (c), shows the mechanical solution adopted to allow that the four capstans were mounted on the same side with respect to the $z_0 - z_2$ plane. The hollow shaft, which insists on the main RU axle through a couple of steel ball bearings, yokes both the external capstans (in red). At the same time, the hollow shaft supports the internal capstans pair (in green) through a couple of thin steel ball bearings.

3.3 Wrist Interface Design

The WRist ExoSkeleton (WRES) is a purely rotational 3 DoF forearm-wrist exoskeleton based on serial kinematics (shown in figure 4 and in figure 5), and powered by BLDC gear motors. The device is able to elicit torques on the users' articulations: forearm pronation/supination (PS), wrist flexion/extension (FE) and radial/ulnar deviation (RU). The design process has considered the wrist articulations to intersect in a point as the majority of the wrist exoskeletons ([20, 36, 8]), even if it is well known that the complex wrist bones structure is characterized by an ellipsoid joint with an eccentricity between RU and FE axes ([48, 17, 26]).

3.3.1 Requirements

In order to develop ergonomically sound design, an exoskeleton system must conform to natural movements and limitations of a upper human limb. In fact, wrist articulations help the human

perform complex motions of the hand. In particular, by neglecting small deviations of the axes of rotation during the movement, the simplified kinematics of the human forearm and wrist can be modeled as a three DoFs kinematic chain. Hence, the orientation of the hand with respect to the arm can be studied in the 3-dimensional manifold SO(3).

Several studies have been carried on in providing normal standards for the functional range of motion (RoM) of the wrist during typical activities of daily living (ADL). In [43], a group of 40 healthy subjects was examined to define the ideal RoMs required to perform ADL, resulting in 40°for both dorsiflexion (or extension) and palmar flexion (or simply flexion), 30°of ulnar deviation, and 10°of radial deviation, which reflects the 70% wrist motion required for ADL. As reported in [53], the usual RoM for PS vary from 80°to 90°respectively. The magnitude of radial deviation reaches up to 25°, while ulnar deviation reaches the amplitude up to 45°, when the wrist is in the neutral location about FE. In its turn, FE motions have a range of up to 80°and 50°respectively, with the wrist in the neutral position about RU. The required torques for the ADL vary from 0.06 to 0.35 Nm, as reported in [38]. Further main requirements concern the lightness of the device, its easiness to be worn, and the need to have an open structure in order to allow the user to manipulate real objects or avoid collision between the upper bilateral arms exoskeleton ALeX, during bimanual operational task.

3.3.2 Kinematics & Mechanical Design

The basic kinematics structure of WRES, depicted in figure 5a, is characterized by a spherical 3DoF kinematics based on serial configuration, that allows quasi-full RoM for the human wrist. Serial kinematic configurations have the advantage not only to lead to simpler mechanical structures, but also to obtain a device ease to be worn by the user.

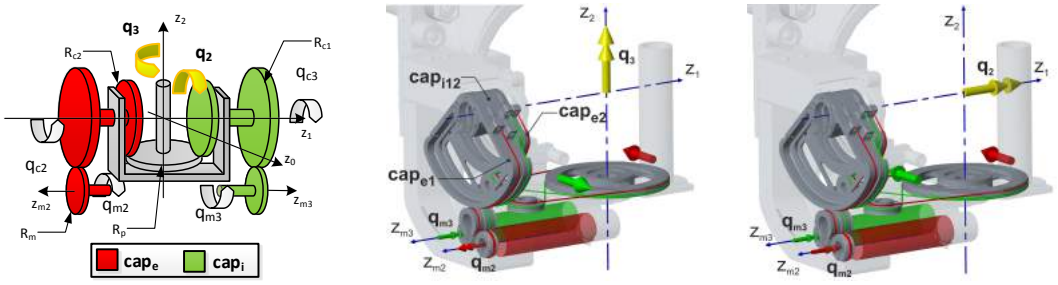

Figure 6: The schematic representation of differential transmission kinematics and the main geometric parameters are reported in (a), where: $R_{c1} = 69.5mm$ the driving capstan radius, $R_{c2} = 46mm$ the driven capstan radius, $R_p = 46mm$ the differential pulley radius and $R_m = 10mm$ the motor drum radius.
The two CAD model representations shows the cable routings for the motors 2 and 3. In (b) is shown the configuration for $q_{m2} = |q_m|$ and $q_{m3} = -|q_m|$, that results in $\boldsymbol{q_{FE}} = [0 \quad q_3]$, whereas in (c) for $q_{m2} = -|q_m|$ and $q_{m3} = -|q_m|$, we obtain $\boldsymbol{q_{RU}} = [q_2 \quad 0]$.

The WRES interface is a mechanically compliant robotic device, actuated by means of electric BLDC gear motors with optical encoders. For WRES, the total weight is about 2.9 Kg including drivers box, of which about 1.8 Kg are due to the moving parts. Anodized aluminum alloy 7075-T6 has been used for most of the mechanical parts, due to its good tradeoff between high stiffness and lightness.
The PS joint has been designed to improve the wearability of the wrist device, by using an open

curvilinear rail and rolling slider solution. Two $180\,\mathrm{deg}$, 127mm diameter rail circular segments are mounted on both side of the moving cylindrical open hub. Two slider mechanisms, each mounted to a fixed frame, are used to support the required moment loads.
The actuators 2 and 3 are remotely located with respect to the end-effector, both mounted on the link 1, in order to achieve the highest possible dynamic performances compatibly with a simple configuration for the cable routing of differential transmission.
The kinematics adopted in the last two DoF (RU and FE) of WRES combines the output motion of two parallel actuators by using a differential transmission, where the output, the joint variables q_2 and q_3, are given by the linear combination of the two motor variables, q_{m2} and q_{m3}, given by the relationship reported in the equation 1.

Figure 6a shows a schematic representation of the transmission kinematics and the geometric notation adopted for its description. Both the motors act in parallel on the central main pulley through a double-stage pulley transmission each. For compactness purpose and to make the structure open and easy to be worn by the user, two double-stage transmissions (named in figure 6a as cap_i and cap_e for the internal and external one, respectively) have been arranged on the same side, with respect to the $z_0 - z_2$ plane.

The first-stage pulley transmission for each motor is given through the capstans cap_{e1} and cap_{i1} (namely, driving capstans). The external capstan pair (red in figure 5c) is coupled through a hollow shaft, whereas the internal ones (green in figure 5c) are coupled rigidly.Both capstans, $2e$ and $2i$, drive directly the pulley of the link 3, and the link 2.
The 2 DoF, FE and RU, are actuated by means of the differential transmission, where the concurrent motion of both the capstan pairs cap_e and cap_i produces the rotation of link 2 and 3 around the horizontal axis z_1 (in figure 6c). The opposite motion of the capstan pairs produces a rotation of only the link 3 around the vertical axis z_2 (in figure 6b).

The relationships between joints and motor angles, due to the differential transmission, are given by the reduction matrix:

$$\begin{bmatrix} q_1 \\ q_2 \\ q_3 \end{bmatrix} = \begin{bmatrix} 1/\tau_1 & 0 & 0 \\ 0 & -1/2\,\tau_2\,\tau_3 & -1/2\,\tau_2\,\tau_3 \\ 0 & -1/2\,\tau_2\,\tau_3 & 1/2\,\tau_2\,\tau_3 \end{bmatrix} \begin{bmatrix} q_{m1} \\ q_{m2} \\ q_{m3} \end{bmatrix} \tag{1}$$

where $\tau_1 = R_1/R_m = 8.8$ represents the transmission ratios for the single-stage of capstan tendon transmission for PS joint ($R_1 = 88mm$ the PS capstan radius), $\tau_2 = R_p/R_{c2} = 1$, the second-stage of differential transmission and $\tau_3 = R_{c1}/R_m = 6.95$, the first-stage of differential transmission.
Given the equation 1, the positive direction of the joint q_2, reported in figure 6c, is given by the sum of negative contributions from both actuators, whereas the positive direction of the joint q_3 is given by the sum of the negative contribution from the actuator 3, and positive contribution from the actuator 2, as shown in figure 6b
This kind of transmission makes the operation of device symmetric with respect to two possible motions of the hand exos (flexion/extension and radio-ulnar joints), achieving high kinematic isotropy along these directions. As shown in figure 6, the torque transmission from the actuators to the FE and RU joints is achieved through in-tension stainless steel cables (1mm of diameter, 7x19 strand core) routed among drums, capstans and idle pulleys. Such a configuration allows for a high performance open loop force control without the use of costly force/torque sensors located at the end-effector of the manipulator or at its joints. The cables are pre-tensioned by using through-hole screws, and nuts are used to prevent cable loosening.

Table 1: WRES capabilities compared with the requirements for ADL (averaged over the data from [15, 2, 43, 38]) and the most recent wrist devices (IIT Wrist Device [8], WG [33], Open Wrist [39], RiceWrist-S [37], RiceWrist-Parallel [20], CADEN7 [38]).

	ADL	IIT-WD	WG	OW	RW-S	RW-P	C7	**WRES**
Joint	M $[95\% C.I.]$	Range of Motion [deg]						
PS	127.3 $[91.2, 163.4]$	160	180	170	180	180	155	**146**
FE	100.3 $[82.4, 118.2]$	144	180	135	130	84	120	**75**
RU	47.8 $[29.6, 66]$	72	60	75	75	52	60	**40**
Joint		Max Continuous Torque [Nm]						
PS	0.06	2.77	2.87	3.5	1.69	5.08	N.A.	**6.52**
FE	0.35	1.53	1.77	3.6	3.37	5.3	N.A.	**1.62**
RU	0.35	1.63	1.77	2.3	2.11	5.3	N.A.	**1.62**

3.4 Electronics and Control Design

This section describes the control electronics and the control architecture of the wrist device.

3.4.1 Hardware Setup

Each of the three BLDC gearmotors is controlled by a digital EtherCAT drive (Neptune Ingenia Drive, www.ingeniamc.com). The current loop on each drive is designable and runs at 10 kHz. The main control of the whole wrist device is executed on a generic personal computer with Simulink Real-Time as Operating System at 5 kHz.

3.5 Control Scheme and Gearmotor Identification

The low-level control of the wrist exoskeleton takes into account two main feed-forward compensation terms: the gravity compensation and gearmotors viscous friction compensation. The viscous friction due to the transmission system has been neglected since all the pulleys and links are mounted on ball bearings. Figure 7 shows the low-level control scheme where, τ_j^C and τ_m^C

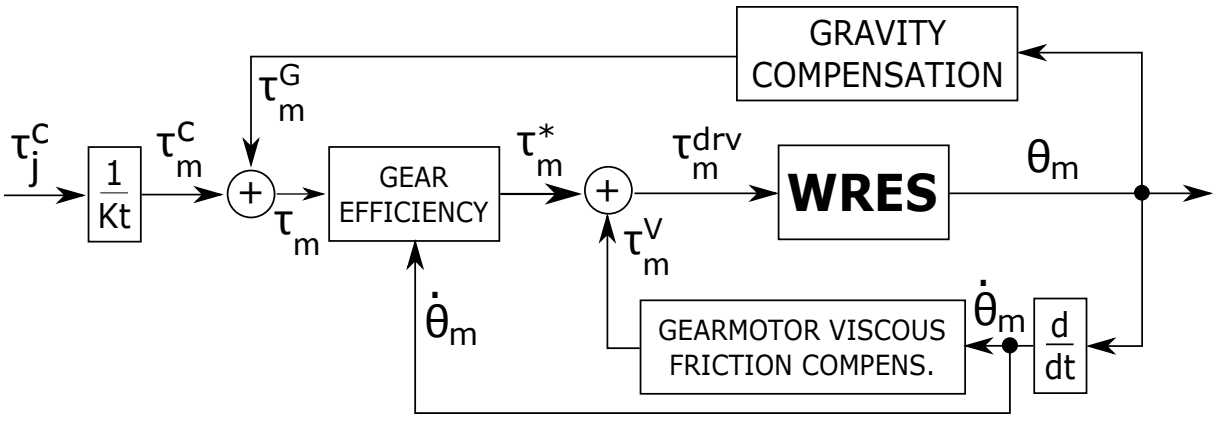

Figure 7: **Low-level control scheme.**

are the joint and motor control torques, τ_m^G and τ_m^V are the two motor torques to compensate the link weights and the gearmotors unit viscous friction, τ_m^{drv} is the reference motor torque sent to the driver, θ_m and $\dot{\theta}_m$ are the motor position and speed, respectively. Finally, the τ_m^* takes into account the gearhead efficiency and it is computed as follow:

$$\tau_m^* = \begin{cases} \frac{\tau_m}{\eta_D}, & \text{if } \tau_m \dot{\theta}_m > 0 \\ \eta_I \tau_m, & \text{if } \tau_m \dot{\theta}_m < 0 \end{cases} \tag{2}$$

where $\eta_I = \frac{2\eta_D - 1}{\eta_D}$, η_D and η_I are the direct and indirect efficiencies of the gearhead.

The analytic gravity compensation model considers the device as a simple serial robot with three rotational joints also including the internal motion of the capstans. As above, the gearhead efficiency (both direct and indirect efficiencies) has been taken into account to compensate for the gearmotor behavior when it acts as motor or brake. For this reason, a set of experiments has been conducted to identify the gearhead efficiency and the viscous friction of the gearmotors and the torque constant of the motors.

As a first step, for torque constant identification, different loads have been applied on the gearmotor shaft by using a pulley. In detail, the motor current required for equilibrating the external loads has been recorded during the clockwise (CW) and counter-clockwise (CCW) slow rotations, hence against and in favor of the gravity. The motor torque constant (K_m) has been modeled as the slope of the curve obtained averaging the two load torque-current characteristics acquired during CW and CCW rotations (Fig.8). Then, the direct gearhead efficiency has been computed by dividing (K_m) by the slope of the curve load torque-current acquired during the rotation made against gravity.

As a second step, the estimated motor torque has been acquired at different motor speeds (both CC and CCW) without any load. The experimental torque-speed relation (that is the viscous friction) has been modeled as a simple multi-linear function (Fig.8).

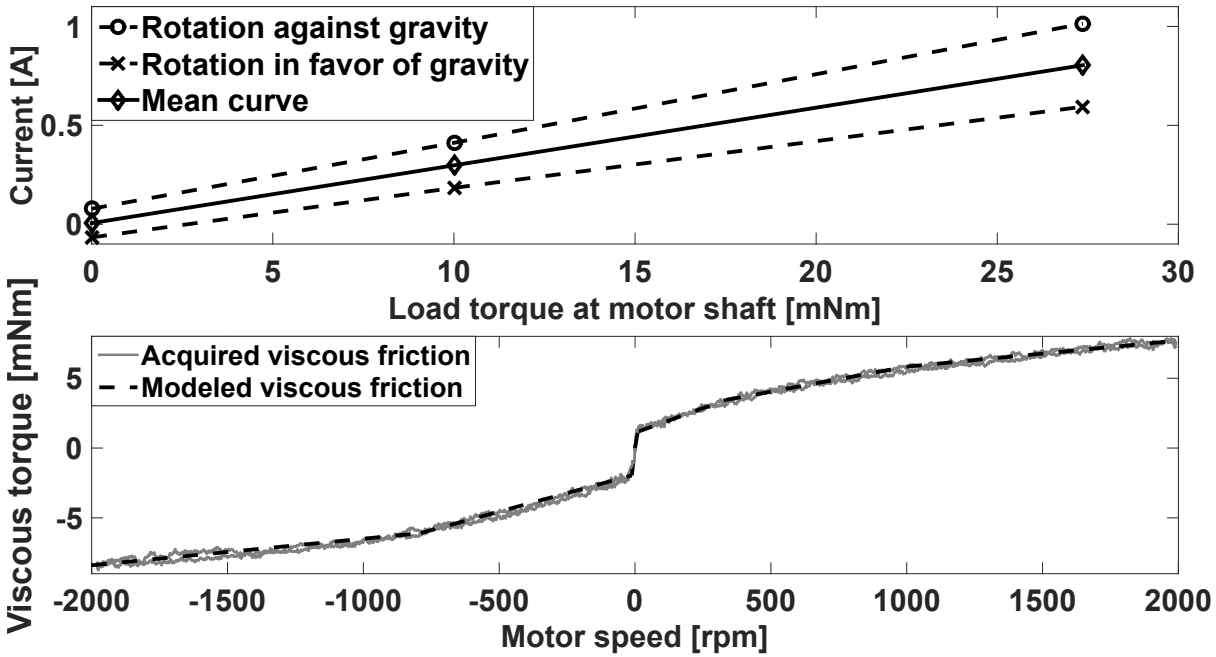

Figure 8: **Joint 1 gearmotor data. (Top)** Currents-load torque curves. **(Below)** Experimental and modeled viscous friction.

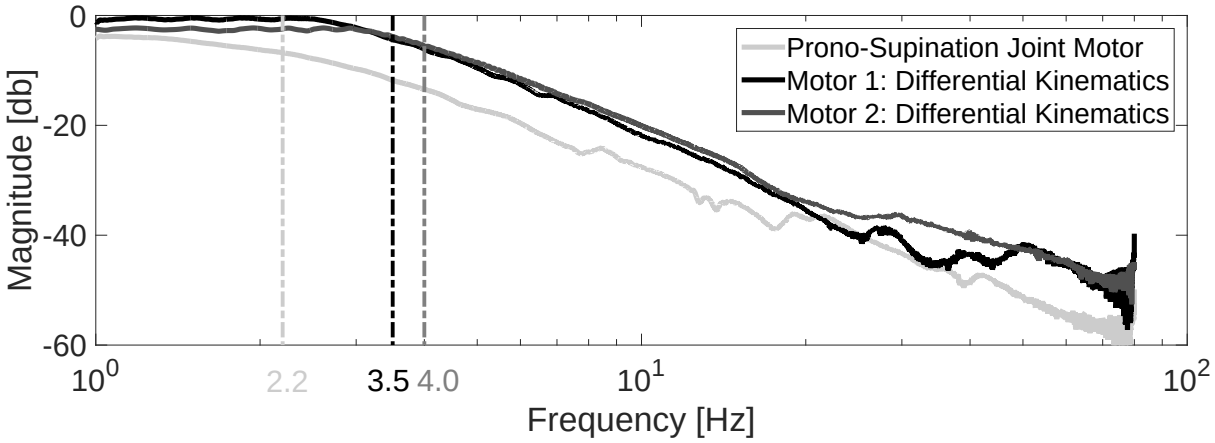

Figure 9: **Dynamic Responses.** The magnitude (dB) of the transfer function $G(s) = \theta_m(s)/\tau_m(s)$ for each of the three gearmotors, where θ_m is the measured motor angle expressed in radians and τ_m is the estimated motor torque expressed in Nm. 2.2 Hz, 3.5 Hz and 4.0 Hz are the bandwith values individuated with the -3dB rule.

3.6 WRES Experimental Evaluation

Two different experimental sessions have been performed: the first consisted in experimental measurements aiming to characterize bandwidth, and the static friction of each WRES joints. The resulting exoskeleton system was then evaluated by means of an haptic rendering application. The experimental application evaluated both system transparency in free movements and interaction with a virtual wall.

A set of experiments has been conducted to evaluate the performance of the proposed device. Firstly, the dynamic response of WRES has been evaluated. In detail, for each motor, a logarithmic chirp torque signal ranging from 1Hz to 80Hz has been fed to the motor driver. The result of the dynamic response of each gear motor is reported in Figure 9.

Static friction was then measured at each joint and at different joint angular positions. For each measurement, the joint was positioned using a closed-loop position control. Once the position of the joint was stabilized, the closed loop control was turned off and a feed-forward slow ramp (0.05 Nm/s at the joint) was fed as torque reference to the joint. The value of the torque was recorded when a displacement of 0.5 deg was recorded. Since gravity compensation was in force, for each measurement the test movement was operated twice in opposite directions and the value of the torque was averaged. Static friction measurements were performed on a set of eleven different joint angular positions, spanning the full range of each joint, and repeated five times for each position. Results of the static friction measurements are shown in Figure 10.

Following the experimental characterization of the system, we evaluated the transparency of the device, hence the accuracy of the feed-forward terms that are compensated into the low-level control: the gravity torque and the gear motor viscous friction torque compensations. A six-axis force/torque sensor (ATI Gamma - www.ati-ia.com) was mounted at the base of the device handle to measure the interaction torques between the user and the haptic device. One subject was then asked to wear the wrist exoskeleton and perform several joint rotations, at different speeds, for each of the three joints. Figure 11 reports the data acquired in this phase.

The WRES was finally implemented in a virtual haptic rendering application in order to validate the overall functionality of the system. As explained in the sketch in Figure 12ca, the haptic rendering application involved a virtual environment (VE) simulating interaction

between a stick held by the user's hand and a four walled box. Distance of the stick from the center of rotation of the wrist in the VE matched the real dimensions of the WRES handle (60 mm distance, 200 mm height of the tip). The stiffness and the viscous friction of the walls properties have been defined in the Cartesian space: the stiffness and viscous coefficient were set to 1.5 N/mm and 15 Ns/mm^2. Similarly to the previous experiment, interaction forces and torques between the WRES and the user were measured through the six axis force sensor mounted at the handle (sensor was used just for measurement and did not fed any information to the WRES control). Figure 12c shows results related to one subject exploring the boundaries of the virtual three times. Forces and torques measured by the force sensor, and reference forces generated by the virtual wall were both transposed to the three-dimensional space of the WRES base frame, and shown in bottom graphs of Figure 12c.

3.7 Discussion

Characterization of the WRES underscores the significance of the numerous design considerations. Considering the data reported in Table 1 it emerges that the WRES joint range of motions and maximum continuous torques are consistent with the values required during the activities of daily living. The main effect of the strict design requirements (extensively discussed in Sec. 3.1) is the reduced RoMs compared to most recent devices (Table 1). On the other hand, the compactness and the high force-volume and force-weight ratios ensure joint maximum continuous torques consistent with the averaged values of other existing devices (Table 1).

Analyzing the results of the static friction identification and the transparency tests, it can be stated that the final device has respected the requirement of being an impedance-type device. The FE joint showed lower friction than the RU joint (FE 0.133 ± 0.004 Nm, RU 0.223 ± 0.025), since it does not involve the internal movement of the differential mechanism as for the RU joint. Friction of the PS joint, implemented through the circular guide, was 0.572 ± 0.130. Figure 10 also shows that static friction increased for higher angular position of the PS joint: this trend is explained by the different direction of the gravity force and of the resulting momentum applied to the bearings of the circular guide. In Figure. 11 it is worth noticing that, although the joint speeds reached very high values (up to 60 deg/s for PS and RU joints and up to 200 deg/s for FE joint), the module of the interaction torque is less than 0.8 Nm for the PS joint, 0.3 Nm

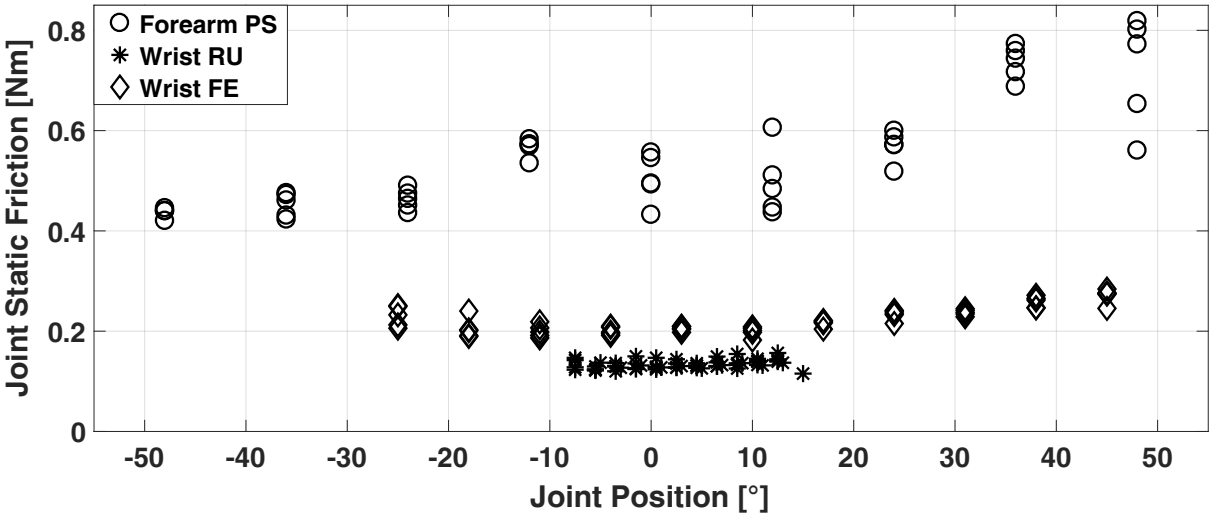

Figure 10: **Static Friction.** Static friction measured for each joint and at different joint positions. Each point is the average of two test movements in opposite directions.

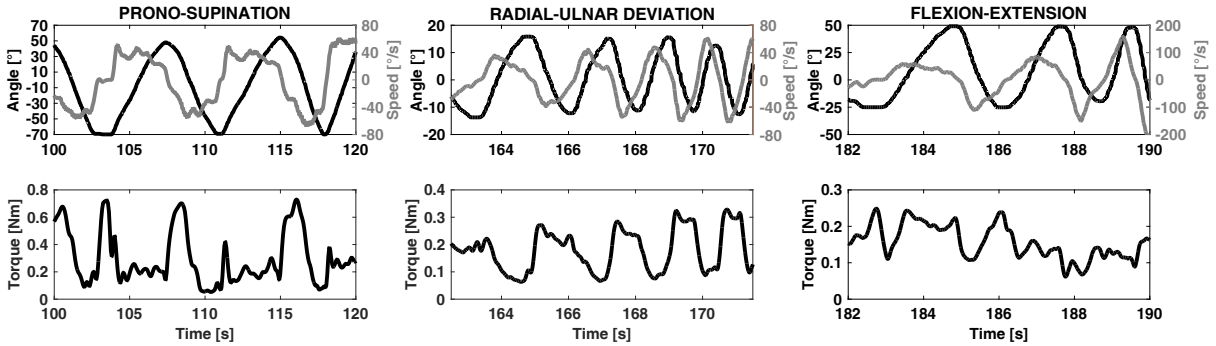

Figure 11: **Transparency evaluation**. At the top row, the joint angle and speeds measured during the acquisition are reported for each of the three wrist joints. At the bottom row, the module of the total torque applied at wrist center of rotation.

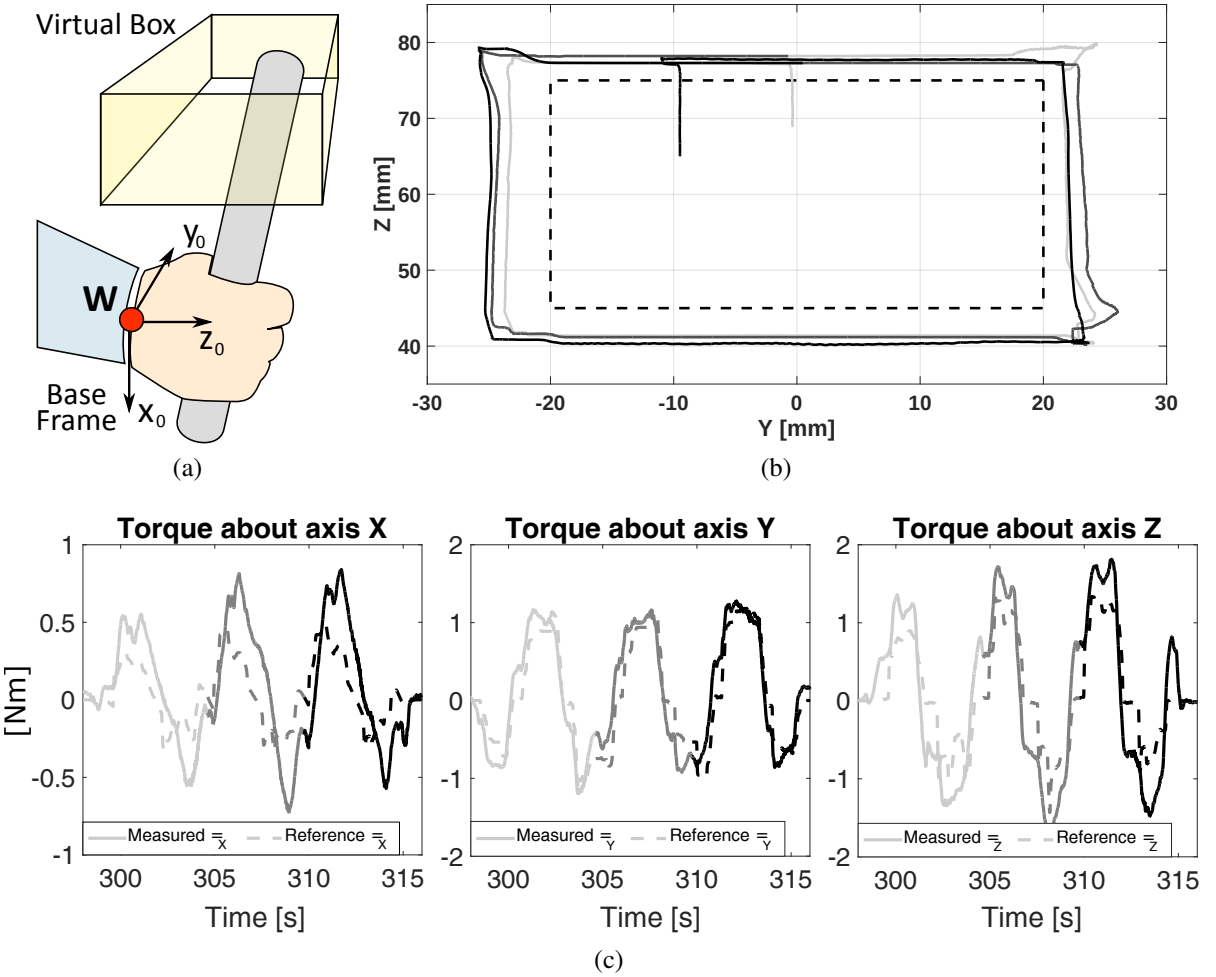

(a) (b) (c)

Figure 12: **Haptic rendering.** (a) Scheme of the implemented haptic rendering application, involving interaction with virtual walls. (b) Position in the Cartesian coordinates of the end effector (solid lines) interacting with virtual walls (dotted line) during exploration of the wall perimeter performed by a human user. (c) Measured interaction torques (solid lines) and reference torques (dotted lines) generated by the virtual wall in the base frame. Different grayscale colors indicate different loops of exploration of the box perimeter.

Figure 13: Integration of WRES interface on a upper arm exoskeleton.

for the RU joint and 0.3 Nm for the FE joint. The PS presents higher interaction torque values over time; this feature is motivated by both the higher inertia of the link 1 and the higher static friction of the PS joint as shown in Figure. 10.

Results in Figure. 12cc show consistency of the whole system in the haptic rendering. Regarding performance of the haptic rendering, the RMSE between reference and measured torques at the base frame were: X: 0.270 Nm, Y: 0.271 Nm, Z: 0.500 Nm. The values of the measured RMSE errors of each axis are comparable with values of static friction measured in the previous experimental session. Static friction could not be compensated in the adopted sensorless control approach: bottom graphs of Figure 12c (in particular for axis X and Z) also show how error between the reference and the measured torque was higher in regions with higher interaction forces with the virtual wall and lower velocities along the specific axis.

As shown in Figure 13, the wrist exoskeleton WRES has been integrated with the fully actuated four DoFs ALEx exoskeleton and the hand exoskeleton. As required, the hand palm is free to interact with any real object. Moreover, from the Figure 13 it can be noted that if the user worn the complete left exoskeleton arm, he would be easily able to interact with real and virtual objects. Future works will focus on the improvement in the design, focusing on the weight reduction and a more ergonomics physical interface.

4 Hand Exoskeleton Module

Hand exoskeletons are widely used for rehabilitative, assistive and teleoperation applications [23]. Two important issues to be addressed in their design are ergonomics and safety: these two requirements are mapped in functional design specifications, that are correspondingly reduced weight and bulk of the device, considering that the human hand has a high number of degrees of freedom (DoFs) and alignment of exoskeleton center of rotations with human joints to prevent the generation of internal loads. This coincidence can be achieved by means of outer structures to the phalange, that limit somehow the wearability of the devices, or through remote center of rotation or multi-loop mechanisms. In fully controlled exoskeletons, all finger joints are controlled independently but this poses an issue in terms of high cost and mechanical complexity. For this reason, the number of DoFs for the exoskeleton is typically reduced by adding kinematic coupling among joints through additional linkages to couple the joints implicitly [1, 51, 14, 42]. Alternatively, the flexion-extension movement of each phalange can be reduced to a single DoF by attaching the exoskeleton to the fingertip only [4, 5, 18, 21, 50]. In both strategies, the relation between finger joints guided by the exoskeleton is coupled anatomically or mechanically.

An interesting approach to overcome the previously defined relation between finger joints is the adoption of an underactuation [13, 47]. The underactuated hand exoskeletons utilize less number of actuators than number of DoFs, by introducing extra DoFs to the mechanism through passive joints and/or elastic elements [27]. Although the implicit control of finger joints cannot be achieved, the overall pose is reached based on the interaction forces. The use of underactuation improves the simplicity and affordability of the exoskeletons, but suffers from the lack of controllability.

The lack of controllability of underactuated devices is currently an active research topic for haptics point of view. Luecke [31] and Meli and Prattichizzo[34] developed different strategies for Cartesian devices, where all DoFs are designed independently, during certain tasks. However these strategies cannot be generalized to improve the performance of underactuated hand exoskeletons, since the motivation is to achieve multi DoFs using less actuators. Previously, a proxy-based rendering strategy for multi-dimensional haptic simulations has been developed [30]; even though the proposed strategy is shown to be effective in the haptics point of view and more stable compared to the conventional methods, the multi-dimensional approach is redundant for rendering strategies from the control perspective.

SSSA defined two rendering strategies to minimize the error between perceived and desired forces or position and investigates their impact on a trajectory tracking task. Instead of working in a multi-dimensional simulation environment [30], the control problem is reduced to the physical mobility of the system. The basic idea behind these strategies is to analyze the capabilities and mechanical constraints set by the underactuated device and adjust the rendered forces accordingly. Both methods will be tested and compared in real life in terms of their pose and rendered force accuracy.

4.1 Underactuated Hand Exoskeletons

The underactuated hand exoskeletons are characterized by a higher number of DoFs than actuators using passive elements. Such an extra mobility allows the mechanism to adjust its behavior automatically based on the interaction forces while the user, who wears the exoskeleton, grasps objects with different shapes and sizes. Even though these devices do not have the ability to fully constrain a given posture control of the fingers, they can complete complex grasping tasks

simply by controlling the direction to open/close the finger as depicted in Fig. 14.

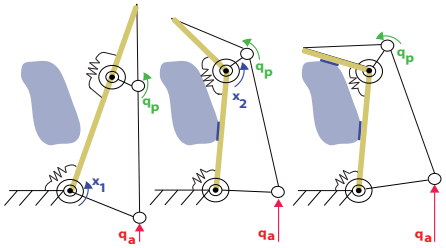

Figure 14: Underactuation concept during grasping using a 2 $DoFs$ underactuated system with a single actuator: q_a, q_p and $\boldsymbol{x} = (x_1, x_2)^T$ represent the actuated and non-actuated input and output finger joint displacements.

4.1.1 Control Structure

The pose of a generic underactuated hand exoskeleton can be expressed using input joints as $\boldsymbol{q} = (\boldsymbol{q}_a, \boldsymbol{q}_p)^T$, where $\boldsymbol{q}_a$ and $\boldsymbol{q}_p$ represent the active (actuated) and passive (non-actuated) joints. The input forces that are supplied to the mechanism can be defined as $\boldsymbol{\tau} = (\boldsymbol{\tau}_a,\ \boldsymbol{\tau}_p)^T$ with active and passive components of input joints $\boldsymbol{q}$. Similarly, the output finger joints $\boldsymbol{x}$ defines the pose of the finger. The forces applied to the output joints by the mechanism can be expressed as $\boldsymbol{\gamma}$, such that $dim\ (\boldsymbol{\tau}) = dim\ (\boldsymbol{\gamma}) > dim\ (\boldsymbol{\tau}_a)$ due to the underactuation. The kinematic mapping between the exoskeleton and finger joints is formulated by the Jacobian $\boldsymbol{J} = (\boldsymbol{J}_a,\ \boldsymbol{J}_p)$, defined by the equation:

$$\dot{\boldsymbol{x}} = \boldsymbol{J}\ \dot{\boldsymbol{q}} = \begin{bmatrix} \boldsymbol{J}_a & \boldsymbol{J}_p \end{bmatrix} \begin{pmatrix} \dot{\boldsymbol{q}}_a \\ \dot{\boldsymbol{q}}_p \end{pmatrix} \tag{3}$$

where $\boldsymbol{J}_a$ and $\boldsymbol{J}_p$ are related to the active and the passive joints, respectively. Jacobian can also be used to relate input and output forces as $\boldsymbol{\tau} = \boldsymbol{J}^T\ \boldsymbol{\gamma}$.

The active joints of an underactuated hand exoskeleton can be controlled by a simple position control to perform a generic grasping task. Yet, neither the forces being applied on the finger joints, nor the pose of the finger can be controlled. Alternatively, an impedance control around the finger joints can determine the actuation effort for a desired pose of the finger, both for interaction with virtual environments and motion assistance in rehabilitation applications. The desired forces around finger joints can be defined based on user's activity in the operational space using Eqn. (4), where $\boldsymbol{x}$ and $\boldsymbol{x}_d$ represent the instantaneous and the desired finger pose. $\boldsymbol{K}_i$ is the diagonal, controllable stiffness matrix to render the impedance control.

$$\boldsymbol{\gamma}_d = \boldsymbol{K}_i\ (\boldsymbol{x}_d - \boldsymbol{x}) \tag{4}$$

The required input forces to render the desired output forces ($\boldsymbol{\gamma}_d$) can be calculated using Jacobian $\boldsymbol{J}$. The detailed mapping between the desired forces to be rendered and desired input forces can be expressed as

$$\begin{bmatrix} \boldsymbol{\tau}_{ad} \\ \boldsymbol{\tau}_{p_d} \end{bmatrix} = \begin{bmatrix} \boldsymbol{J}_a^T \\ \boldsymbol{J}_p^T \end{bmatrix} \boldsymbol{\gamma}_d \tag{5}$$

where $\boldsymbol{\tau}_{ad}$ and $\boldsymbol{\tau}_{p_d}$ represent the desired force values that need to be applied by the active and passive input joints in order to achieve the desired output forces $\boldsymbol{\gamma}_d$.

4.2 Rendering Strategies

Eqn. (5) computes a full force vector $\boldsymbol{\tau}$, while only on the active joints the underactuated device can apply forces/torques $\boldsymbol{\tau}_a$. In other words, the passivity of the non-actuated input joints ($\boldsymbol{\tau}_p = 0$) imposes a strict relation between the output joint torques $\boldsymbol{\gamma}$ that defines the force distribution of the underactuated device. Therefore, the actuation forces might fail to render $\boldsymbol{\gamma}_d$ in case they do not satisfy the given underactuation constraint and result in a different set of perceived forces ($\boldsymbol{\gamma}$). To reduce the effect of the difference between $\boldsymbol{\gamma}_d$ and $\boldsymbol{\gamma}$, rendering strategies can be developed. Generally speaking, these strategies aim to compute a proxy set of output forces ($\boldsymbol{\gamma}^*$) that satisfies the underactuation constraint with different approaches. Ensuring the underactuation constraint to be satisfied, the forces perceived by the user can be estimated and optimized according to the operative task.

Proxy forces $\boldsymbol{\gamma}^*$ can be calculated by developing rendering strategies in the force and the operational spaces. The strategy in the force space aims to find $\boldsymbol{\gamma}^*$ by searching the closest distance to $\boldsymbol{\gamma}_d$, while the strategy in the operational space defines a desired position proxy $\boldsymbol{x}^*$ by estimating the finger pose which will be reached by the user based on his previous behavior, and compute $\boldsymbol{\gamma}^*$ using the impedance control approach in Eqn. (4). In both strategies, the proxy sets are ensured to satisfy the relation $\boldsymbol{\tau}_p = 0$.

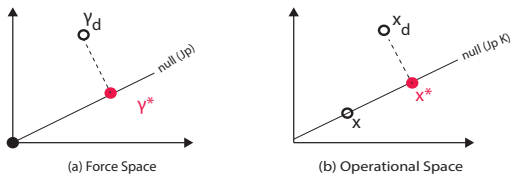

Figure 15: Rendering algorithms (a) in the force space, where proxy $\boldsymbol{\gamma}^*$ is the closest point to $\boldsymbol{\gamma}_d$ on $null(\boldsymbol{J}_p)$, which passes from the origin and (b) in the operational space, where $\boldsymbol{x}^*$ is the closest point to $\boldsymbol{x}_d$ on $null(\boldsymbol{J}_p\ \boldsymbol{K})$, which passes from $\boldsymbol{x}$.

Rendering Strategy in the Force Space The rendering strategy in the force space aims to define a proxy $\boldsymbol{\gamma}^*$ with minimum distance to $\boldsymbol{\gamma}_d$, obtained by Eqn. (4), projecting $\boldsymbol{\gamma}_d$ on the null space of $\boldsymbol{J}_p$. Such a minimization problem can be expressed as:

$$\begin{aligned} \boldsymbol{\tau}_a^* &= \boldsymbol{J}_a^T\, \boldsymbol{\gamma}^*, \text{ with} \\ \boldsymbol{\gamma}^* &= argmin\ \frac{1}{2}\ \|\boldsymbol{\gamma}_d - \boldsymbol{\gamma}^*\|^2, \text{ s.t. } \boldsymbol{J}_p^T\, \boldsymbol{\gamma}^* = \boldsymbol{0} \end{aligned} \tag{6}$$

with the closed form expression as

$$\boldsymbol{\gamma}^* = (\boldsymbol{I} - \boldsymbol{J}_p\, (\boldsymbol{J}_p^T\, \boldsymbol{J}_p)^{-1}\, \boldsymbol{J}_p^T)\, \boldsymbol{\gamma}_d. \tag{7}$$

The corresponding actuator forces ($\boldsymbol{\tau}_a^*$) can be calculated by merging Eqns. (4), (6) and (7) as:

$$\boldsymbol{\tau}_a^* = \boldsymbol{J}_a^T\, (\boldsymbol{I} - \boldsymbol{J}_p\, (\boldsymbol{J}_p^T\, \boldsymbol{J}_p)^{-1}\, \boldsymbol{J}_p^T)\, \boldsymbol{K}_i\, (\boldsymbol{x}_d - \boldsymbol{x}). \tag{8}$$

Passivity The virtual impedance displayed in the joint space with full DoF under the control law in Eqn. (8) can easily be expressed as

$$\frac{\partial \boldsymbol{\tau}}{\partial \mathbf{q}} = -\boldsymbol{J}^T \left(\boldsymbol{I} - \boldsymbol{J}_p \left(\boldsymbol{J}_p^T \boldsymbol{J}_p\right)^{-1} \boldsymbol{J}_p^T\right) \boldsymbol{K}_i \boldsymbol{J}. \tag{9}$$

If $\boldsymbol{K}_i = k\ \boldsymbol{I}_n$ where k is a scalar and I_n is the identity matrix, than the system has only positive or zero eigenvalues and so the system is intrinsically passive.

Rendering strategy in the force space does not only calculate a proxy $\boldsymbol{\gamma}^*$ that can be rendered by the underactuated device, but also ensures that it is the closest to the desired $\boldsymbol{\gamma}_d$. For the applications where the main focus is the accuracy of the rendered forces rather than imposing an accurate desired pose, this strategy should provide the best solution.

Rendering Strategy in the Operational Space The extra mobility introduced by the underactuation design gives an infinite possible finger poses $\boldsymbol{x}$ for a given set of actuated joints $\boldsymbol{q_a}$. Therefore, the upcoming pose that the output joints will reach cannot be controlled due to the underactuation, but an estimation can be performed based on the previous behavior of the system and the environment. For the rendering strategy in the operational space, such an estimation matrix $\boldsymbol{K}_{st}$ can be performed by estimating the finger joint stiffness values $\boldsymbol{K}_{st} = \frac{\partial \gamma}{\partial x}$. Assuming that the user will not change his behavior suddenly, the desired forces $\boldsymbol{\gamma}_{st}$ to cause the finger pose $\boldsymbol{x}$ to reach $\boldsymbol{x}_d$ using the estimated joints stiffness $\boldsymbol{K}_{st}$ can be expressed using Eqn. (10).

$$\boldsymbol{\gamma}_{st} = \boldsymbol{K}_{st} \left(\boldsymbol{x}_d - \boldsymbol{x}\right) \tag{10}$$

As for $\boldsymbol{\gamma}$, with an underactuated device is not guaranteed that $\boldsymbol{\gamma}_{st}$ is a feasible set of forces. The rendering strategy in the operational space aims to compute a proxy pose $\boldsymbol{x}^*$ that has the closest distance to $\boldsymbol{x}_d$ and leads intrinsically to a feasible $\boldsymbol{\gamma}_{st}$ as:

$$\begin{aligned} &\boldsymbol{\tau}_a^* = \boldsymbol{J}_a^T \boldsymbol{K}_i \left(\boldsymbol{x}^* - \boldsymbol{x}\right), \text{ with} \\ &\boldsymbol{x}^* = argmin\ \frac{1}{2} \left\|\boldsymbol{x}_d - \boldsymbol{x}^*\right\|^2, \text{ s.t. } \boldsymbol{J}_p^T \boldsymbol{K}_{st} \left(\boldsymbol{x}^* - \boldsymbol{x}\right) = \mathbf{0}, \end{aligned} \tag{11}$$

where the optimization constraint can be simplified as $\boldsymbol{K}^T \left(\boldsymbol{x}^* - \boldsymbol{x}\right) = \mathbf{0}$, where $\boldsymbol{K} = \boldsymbol{K}_{st}^T \boldsymbol{J}_p$. Once the proxy pose $\boldsymbol{x}^*$ is found, the actuated forces $\boldsymbol{\tau}_a^*$ are computed using Eqn. (4), similar to the previous strategy. The minimization problem with the underactuated constraint can also be expressed using the pseudo-inverse as in Eqn. (12).

$$\boldsymbol{x}^* = \boldsymbol{x}_d - \boldsymbol{K} \left(\boldsymbol{K}^T \boldsymbol{K}\right)^{-1} \boldsymbol{K}^T \left(\boldsymbol{x}_d - \boldsymbol{x}\right) \tag{12}$$

Once the proxy pose $\boldsymbol{x}^*$ are achieved through Eqn. (12), the actuator forces can easily be obtained merging Eqns. (10), (11) and (12).

$$\boldsymbol{\tau}_a^* = \boldsymbol{J}_a^T \boldsymbol{K}_i \left(\boldsymbol{I} - \boldsymbol{K} \left(\boldsymbol{K}^T \boldsymbol{K}\right)^{-1} \boldsymbol{K}^T\right) \left(\boldsymbol{x}_d - \boldsymbol{x}\right) \tag{13}$$

Rendering strategy in the operational space defines a proxy pose that minimizes the pose error, while ensuring that the corresponding proxy output forces can be applied by the mechanism. The proxy pose $\boldsymbol{x}^*$ is claimed to be reachable under the assumption that the user will

maintain his previous behavior. Doing so, even if the output joints cannot be controlled implicitly, the overall control aims to minimize the overall pose error. Even though the error between the desired and actual finger joints are expected to be minimized, the error between desired and transmitted joint torques to be rendered might be greater than the previous strategy.

Passivity If we analyze the virtual impedance displayed in the joint space with full degrees of freedom under control law Eqn. (8), we easily find:

$$\frac{\partial \boldsymbol{\tau}}{\partial \mathbf{q}} = -\boldsymbol{J}^T \, \boldsymbol{K}_i \, (\boldsymbol{I} - \boldsymbol{K} \, (\boldsymbol{K}^T \, \boldsymbol{K})^{-1} \, \boldsymbol{K}^T) \, \boldsymbol{J}. \tag{14}$$

Unlike the previous strategy, the estimation stiffness matrix K_{st} affects the eigenvalues of the virtual impedance directly, therefore the stability cannot be ensured at all times. However, computing the impedance might be useful to adjust the estimation matrix according to the eigenvalues of Jacobian matrix in order to satisfy the passivity.

4.3 Experiments

The proposed rendering strategies will be tested experimentally using the underactuated hand exoskeleton [47], shown in Fig. 16. Even though the hand exoskeleton was designed to support 5 fingers independently, this study will use only the index finger component for simplicity.

Figure 16: Multi fingered underactuated hand exoskeleton.

The kinematics of the chosen hand exoskeleton were designed to assist 2 $DoFs$ of user's fingers by controlling the displacement of a single linear actuator as shown in Fig. 17. The mechanical joints are not aligned with the finger joints intentionally to increase the adjustability of the device for various hand sizes. The novel kinematics allow only the perpendicular forces to be applied to finger phalanges, while tangential forces cause the passive linear sliders, which are placed along the finger phalanges, to move with displacements defined as c_1 and c_2. Not transmitting tangential forces significantly improves the simplicity of connectors between the exoskeleton and user's phalanges.

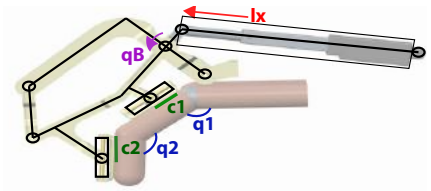

Figure 17: Kinematic scheme of the underactuated finger exoskeleton.

For the given exoskeleton system, the output joints can be defined as finger joint rotations $\boldsymbol{x} = (q_1, q_2)^T$ and the output forces can be expressed as joint torques $\boldsymbol{\gamma} = (\tau_1, \tau_2)^T$. The actuated and non-actuated joint displacement are defined as l_x and q_B.

The implemented finger component is equipped with additional sensors to improve its performance. A potentiometer was utilized to estimate finger pose using forward kinematics in real time [46]. Furthermore, a force sensor was placed between the actuator and the base to achieve closed-loop force control by measuring user's activity. Doing so, the backdriveability is ensured despite of the non-backdriveability caused by the mechanical gearbox inserted within low cost linear actuators.

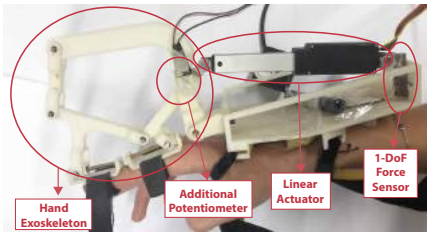

Figure 18: Implementation of the exoskeleton with additional potentiometer for pose estimation and force sensor for active backdriveability.

Using the given exoskeleton, two different tests were performed to show the feasibility of the proposed strategies. The first task imitates a virtual grasping to observe how each strategy behaves. In particular, the user is asked to move freely until he reaches the joint limits, which define a contact with the virtual object, and provides resistive forces after the contact. Even though the feasibility of these methods can be shown with these experiments, they cannot be compared to each other since the user is asked to lead the device and the resulting trajectories are different for each trial. So a second test with a strict position reference was needed to set a comparison between methods. With this motivation, a user study was conducted with 4 subjects while the device is guiding users' fingers to follow a sinusoidal trajectory.

Virtual Grasping Feasibility Tests In the virtual grasping test, a single user was asked to close his finger freely until he perceives the existence of the virtual object. Assuming that the wrist and the hand orientation with respect to the object are kept the same, the grasping can be defined by the joint limits set for finger joints. In this study, the finger joint limits were $\boldsymbol{x}_{lim} = (30^o, 30^o)^T$. Furthermore, the stiffness of the object to be rendered was chosen to be low intentionally, in order to allow the user to exceed the joint limits and observe the rendering strategies to show their work.

The exoskeleton should provide resistance to the user once the joint limits are exceeded during the virtual grasping task and allow the user to move freely before the limits. Such a behavior can be achieved by defining the desired pose $\boldsymbol{x}_d$ as (i) actual pose $\boldsymbol{x}$ before the virtual contact, and (ii) limit pose $\boldsymbol{x}_{lim}$ after the first contact. Then, the desired forces $\boldsymbol{\gamma}$ are calculated for the strategies using Eqn. (4) and Eqn. (10).

Rendering in Force Space Fig. 19 (a) shows user's finger pose $\boldsymbol{x}$ during virtual grasping with fixed joint limits $\boldsymbol{x}_{lim}$. The desired joint torques $\boldsymbol{\tau}_d$ and proxy torques $\boldsymbol{\tau}^*$ were calculated in real time using Eqn. (4) and Eqn. (7) based on desired and actual joints $\boldsymbol{x}_d$ and $\boldsymbol{x}$. The desired and proxy torques for first and second finger joints are presented in Fig. 19 (b) and Fig. 19 (c) correspondingly to highlight the differences. Finally, Fig. 19 (d) shows the measured impedance.

Rendering in Operational Space Similarly, Fig. 20 (a) and Fig. 20 (b) shows user's finger pose $\boldsymbol{x}$ and proxy pose $\boldsymbol{x}^*$ calculated using Eqn. (12) for the first and second finger joints

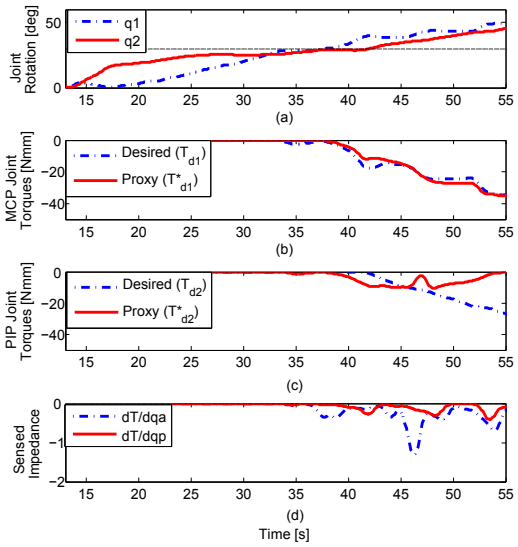

Figure 19: Rendering strategy in the force space.

respectively. As the rendering strategy in the operational space focuses on user's behavior, when the user stops moving (after 102s. in Fig. 20), the proxy pose $\boldsymbol{x}^*$ is set to the desired value $\boldsymbol{x}_d$, ensuring user's stability. Finally, Fig. 20 (c) shows the measured impedance.

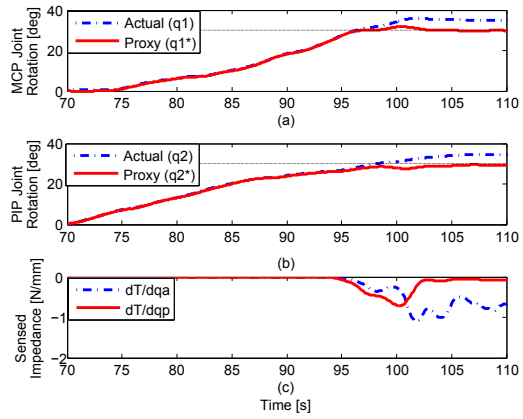

Figure 20: Rendering strategy in the force space.

Discussion The main motivation behind developing these rendering strategies is to improve the force transmission toward the constraint set by the underactuation despite the lack of controllability. The feasibility of these strategies can be claimed only if the proxy forces $\boldsymbol{\gamma}^*$ generated by both strategies can actually be perceived by the user after the mechanical force transmission. During the feasibility tests shown in Fig. 19 and Fig. 20, the interaction forces between the device and the user's finger phalanges are measured using Force Sensing Resistor (FSR) sensors (see Fig. 21) to be compared with desired values. A silicon interface is attached between the FSR surface and user's skin to improve the measurement quality.

The interaction forces measured by FSRs need to be converted to joint torques using the linear displacement of the corresponding finger phalange (c_1, c_2) as depicted in Fig. 17 ($\tau_{FSR} = F_{FSR}/c$). Fig. 22 shows the comparison between actual and proxy joint torques in the (a) force space and (b) in the operational space

Figure 21: FSR sensors between the exoskeleton and user's phalanges for validation of applied torques along the finger joints.

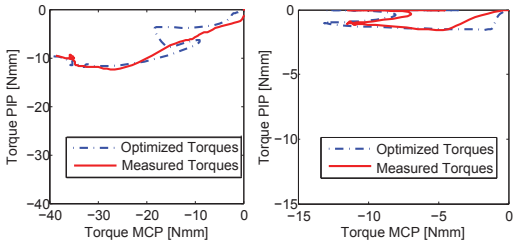

Figure 22: Comparison between the calculated proxy set of desired torques and measured torques through FSR measurements.

The average percentage of root mean square (RMS) error was found to be $1.9177\ \%$ ($0.962\ \%$ and $1.659\ \%$ for the first and second finger joints) using the rendering strategy in the force space and $1.7494\ \%$ ($1.357\ \%$ and $1.104\ \%$ for the first and second finger joints) using the rendering strategy in the operational space. The RMS errors of the proposed rendering strategies are close to each other not to claim any superiority over the other one in terms of ensuring efficient force transmission. In fact, observing that the proxy torques are close to the actual ones show sufficient evidence regarding the efficacy of the force transmission through mechanism due to the ensured passivity constraint. Even though this test can claim the feasibility of both strategies to replace desired values with proxy ones to achieve applicable measures due to the lack of controllability of the device, the comparison between these methods require further tests.

Trajectory Tracking Feasibility Tests The rendering strategy in the force space aims to find a proxy set that minimizes the error between the desired and perceived output forces, while the one in the operational space minimizes the trajectory error between the desired and actual joint pose. A trajectory tracking test calculating the output force and output pose errors for both strategies has been made to verify and compare the performance of the two rendering algorithms.

A sinusoidal reference pose was given as $\boldsymbol{x}_d$ for both strategies and 4 different subjects are asked to wear the device for 3 cycles, as depicted in Fig.23. As the finger exoskeleton opens/closes the finger according to the desired pose, the users were asked to stay in a relaxed behavior.

The RMS values of torque and trajectory errors were calculated between actual and desired values. Fig. 24 shows the average torque error ($\frac{\boldsymbol{\tau}-\boldsymbol{\tau}_d}{\boldsymbol{\tau}_d}$) for different users. Since the proxy torque $\boldsymbol{\tau}^*$ is minimized by the strategy in the force space, it was expected that the torque error using the strategy in the force space was found to be less compared to the one in the operational space. A one-tailed t-test was performed and the p-value was found as $p = 0.05$, which shows significance between the two methods in terms of the torque error.

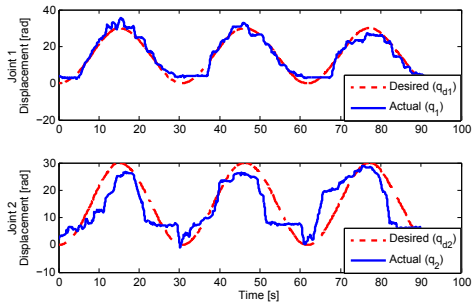

Figure 23: Reference and actual joint displacement of one of the subjects.

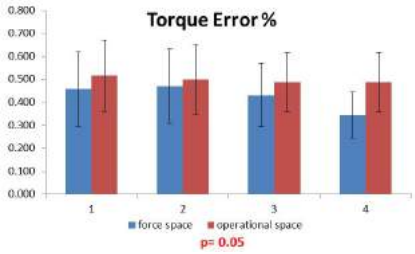

Figure 24: User study comparison for difference between desired and actual finger torque values.

Similarly, Fig. 25 shows the average trajectory error ($\frac{\boldsymbol{q}-\boldsymbol{q}_d}{\boldsymbol{q}_d}$) for different users. Since the proxy pose $\boldsymbol{q}^*$ is minimized by the strategy in the operational space, it was expected that the trajectory error using the strategy in the operational space was found to be less compared to the one in the force space. The one-tailed t-test result was found as $p < 0.002$, which shows the statistical significance between two strategies in terms of trajectory error.

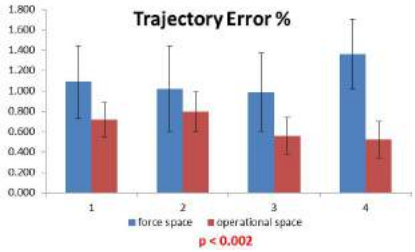

Figure 25: User study comparison for difference between desired and actual finger pose values.

Comparing the trajectory and force errors during a trajectory tracking task shows an observable trend to favor rendering strategies in the force and the operational space, supported by the statistical analyses. In particular, the rendering strategy in the force space can render torques for finger joints similar to the desired values, while the strategy in the operational space can control the finger joints to follow a position reference better despite of the lack of controllability.

4.4 Integration with SVH Robotic Hand

SVH robotic hand is a grasping device designed to behave as close as possible to a human hand (look at figure 26). It is produced by Schunk[1] and distributed by Robotnik company, which

[1]German robotics and automation leader

is specialized on robotic for research. The device features information can be found on their website.

Figure 26: The Schunk 5-Finger Gripping Hand.

Both `Schunk` and `Robotnik` state that `SVH hand` has 20 degrees of freedom. More precisely, Schunk also declares that only nine drivers are responsible for fingers motion, so that all joints[2] can be described by using nine independent variables. Therefore it derives that `SVH hand` is an underactuated system.

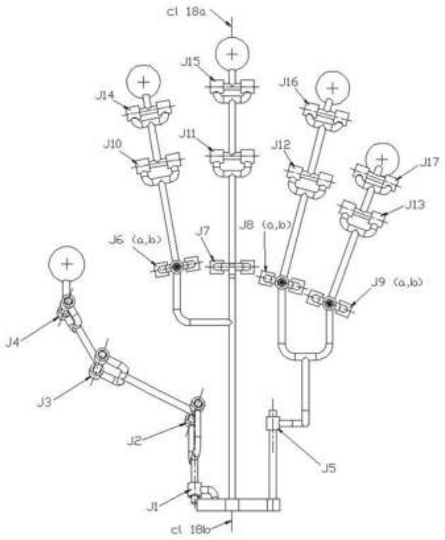

Figure 27: Kinematic diagram of the SVH, showing all 20 joints.

The analysis of the number of joints and DOFs is caused by the mechanical coupling of the joints. The coupling is motivated by the human hand motions, where different joints usually move together, although they are not strictly coupled. [3] This assertion places `schunk svh hand` in a lower level than other anthropomorphic gripping devices like `Shadow Dexterous Hand`.[4]

[2]Schunk SVH hand is composed of 20 revolute joints.

[3]Ruehl, Steffen W., et al. "Experimental evaluation of the Schunk 5-finger gripping hand for grasping tasks." Robotics and Biomimetics (ROBIO), 2014 IEEE International Conference on. IEEE, 2014.

[4]*Shadow Dexterous Hand is based on truly anthropomorphic approach to robot manipulation, approximating human hand kinematics. Using 20 actuated degrees of freedom, and further 4 under-actuated movements posi-*

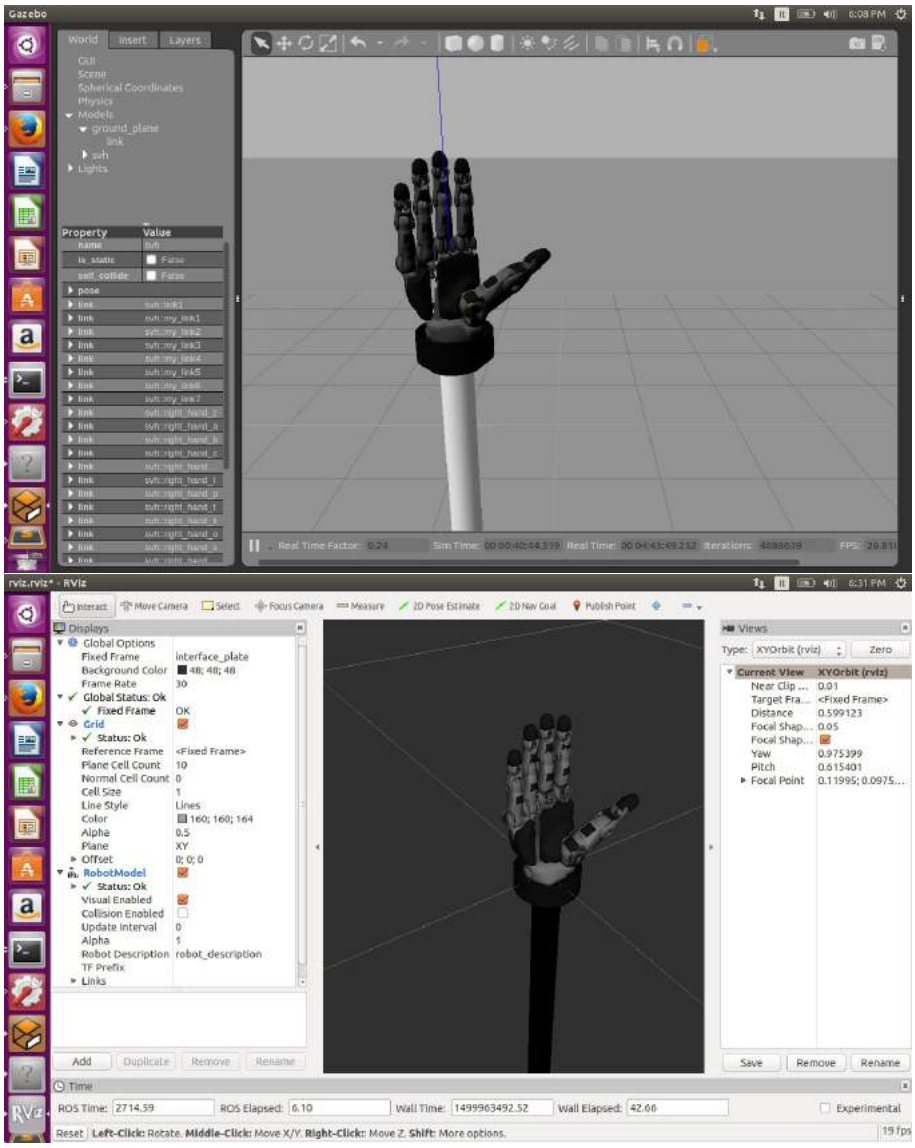

Figure 28: `Gazebo` (on top) and `Rviz` (on bottom) applications. In both cases a `Schunk SVH Hand` model is charged.

According with `SVH Hand` datasheet, `JSPN` controls 9 different variable, one for each hand DoF (look at table 2). But how is the relationship between controlled and total DoF modeled? The trick is performed in `*.xacro` files. `svh_gazebo.urdf.xacro`, which is the file in which all kinematic details are written, contains 20 active revolute joints. 11 joints are declared with the so called *mimic tag*. *Mimic tag* is a special `urdf` tag that specifies the relationship between a measure (like an angle) with another declared in the same model. This procedure allows to exploit `joint_state_publisher` capability to *understand* what are the independent variables of a model and therefore it allows the user to modify only that ones. In conclusion, `svh_gazebo.urdf.xacro` contains a model in which 20 revolute joints are controlled by 9 variable by a hard coded transmission matrix.

tion with force sensors as well as ultra-sensitive touch sensors on the fingertips, the robot hand provides unique capabilities for problems that require the closest approximation of the human hand currently possible. Ruehl, Steffen W., et al. "Experimental evaluation of the Schunk 5-finger gripping hand for grasping tasks." Robotics and Biomimetics (ROBIO), 2014 IEEE International Conference on. IEEE, 2014.

Var Name	**Description**
Thumb_flexion	thumb curvature level
Thumb_opposition	relative position between thumb and the other fingers
Index_distal	index curvature level
Index_proxi	index inclination wrt palm
Middle_proxi	middle curvature level
Middle_distal	middle inclination wrt palm
Ring	ring curvature and inclination
Pinky	pinky curvature and inclination
Fingers_spread	fingers aperture level

Table 2: Control Variable and their meanings.

	Thumb_flex	Thumb_opp	Index_distal	Index_proxi	Middle_proxi	Middle_distal	Ring	Pinky	Fing_spread
j1		1							
j2	1								
j3	1.01511								
j4	1.44889								
j5		1							
j6				1					
j7					1				
j8							1		
j9								1	0.5
j10			1						
j11						1			
j12							1.3588		
j13								1.334	
j14			1.045						
j15						1.0454			
j16							1.42093		
j17								1.42307	
j18									0.5
j19									
j20									1

Table 3: `Schunk_svh_hand` transmission matrix (no number stays for zero). Columns represent controlled variables while rows represent joints. Joint names refers to figure 27.

5 Thumb Exoskeleton

The human hand is the most versatile gripper created by the nature. It is able to firmly grasp objects with different and complex shape thanks to the kinematics of its five fingers, powerful muscles, and a complex biological motor control system. From the kinematic point of view, the hand is composed by a ground part (the palm), four fingers with 4 DoF each, and a thumb. The thumb is the unique finger in the human hand with 5 DoF. Therefore, it is able to perform spatial movements such as its opposition to the other fingers of the hand, which is the basic movement of the grasping action. Because of its incredible complexity, in the last decades, the hand and in particular the human thumb have been widely studied from the kinematic point of view, and many kinematic models able to perform natural motions have been developed. In 1995 Giurintano et al. [16] proposed one of the first 5 link thumb model which entails non orthogonal and non incident axis for the carpo-metacarpal joint (CMC) and metacarpo-phalangeal (MCP) joint. Previous 3-link models use universal joints to model the CMC and MCP joints, leading to a non anatomically correct motion. The comparison between the error produced in the position of the trapeziometacarpal joint by using a 3-link model and a 5-link model has been investigated by Cerveri et al. in [10]. Other studies have been conducted in order to measure muscles arms at the thumb joints [49], or to define some kinematic properties, such as the kinematic parameters of the thumb carpo-metacarpal joint in [11]. An interesting study about the kinematic parameter of the thumb has been performed by Santos et al. in [44]. They investigate the anatomical variability in the Denavit-Hartenberg (D-H) parameters of the human thumb. As results they clustered 3550 D-H parameters sets in four types of five links thumb models. Moreover, the distribution and the representative value for every D-H parameter for each type are provided.

Since hand exoskeletons are developed in order to work combining their kinematics with the kinematics of the hand, the study of the human hand kinematics, especially of the thumb, is of particular interest for the development of effective devices. An example of hand exoskeleton design based on both a hand model and a thumb motion analysis is presented in [7]. Hand exoskeletons can find their application in many different fields, ranging from the rehabilitation to the virtual reality interaction, therefore, in recent years, many hand-exoskeletons have been developed. Some devices have been designed in order to allow full posture control of the finger, therefore, they are able to control all the finger joints independently and provide full mobility during the grasping tasks [29, 22]; however, they mostly suffer from the heavy, bulky and high-cost design, sacrificing the wearability. In alternative one single actuator can be used to control the finger position as proposed in [24], or to control the pose of the fingers constraining the movement of one phalanx to the others, as shown in [12, 28]. Concerning the design of thumb exoskeletons, in literature it is possible to find different solutions proposed for the control of the 5 DoF human thumb. A 2 DoF device for controlling the CMC and MCP joints has been described in [19], whereas in [52], a full 5 DoF device able to control independently all the thumb joints is presented. Finally, in [9] a cable driven underactuated 3 DoF device with two actuators is proposed.

The thumb exoskeleton with the same characteristics of other finger devices but adjusted to the higher complexity of the thumb kinematics has been developed (Figure 29). Data reported in [44] has been used within the design process to create a human thumb model integrated with the designed hand-exos device. The presented device is able to combine the advantages given by a powerful single motor actuation placed on the back of the hand, with a 5 DoF kinematics able to guarantee the full mobility of the users thumb while wearing the device. The single actuation solution allows to reduce the weight and the volume occupied by the actuation system, whereas in order to guarantee the kinematic specifications the proposed device is based on a

parallel kinematics featured by a high degree of underactuation. Furthermore such a parallel kinematics is designed to be able to adapt to different hand sizes. To the best of the author's knowledge, thumb-exoskeletons with such a high degree of underactuation has not been presented in previous works.

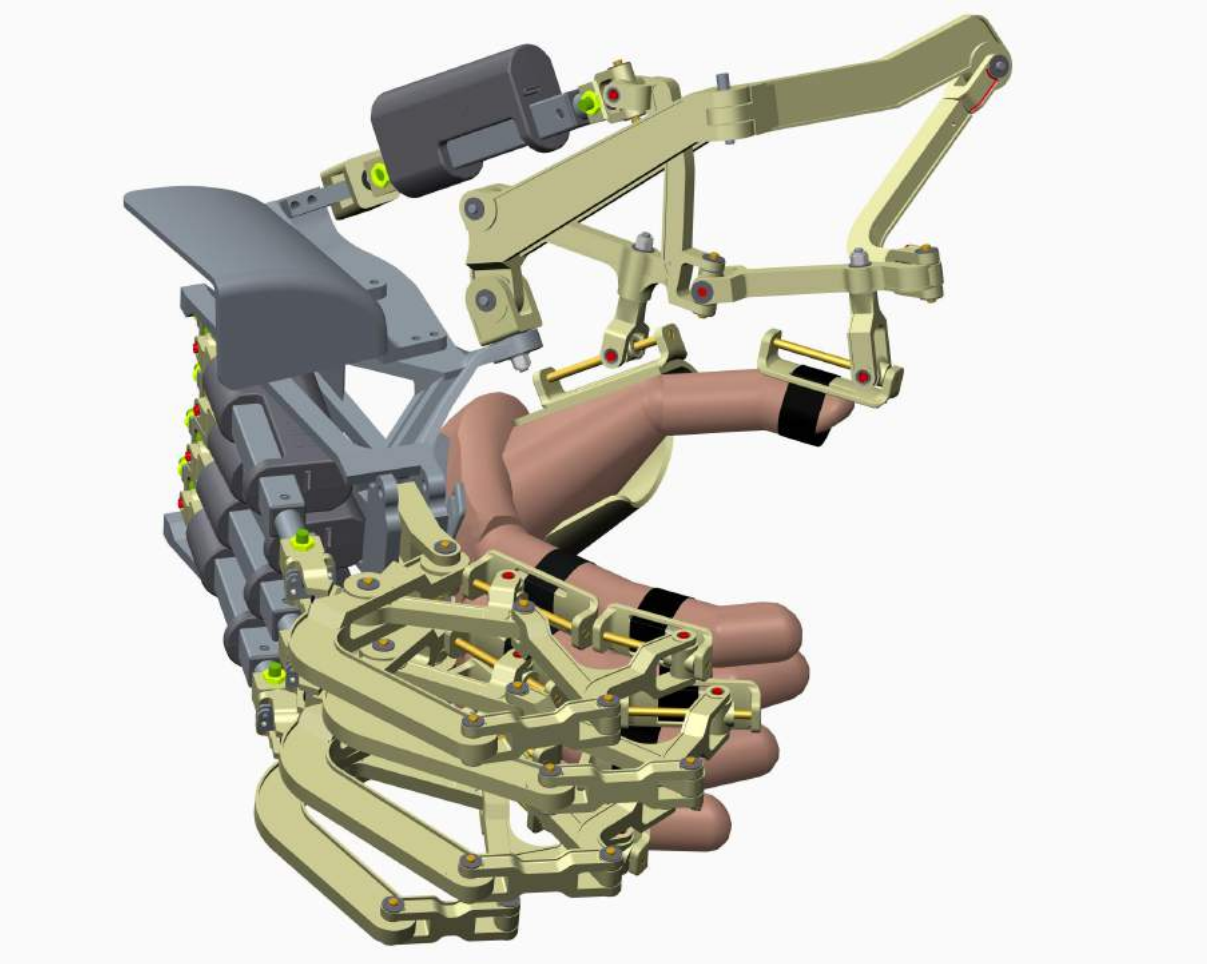

Figure 29: CAD model of the integrated Thumb-exos device with the existing hand exos presented in [45].

5.1 Design Requirements

As mentioned in the introduction the human thumb can be assumed as a serial kinematic chain able to perform complex spatial movements. Accordingly to the most recent literature the results provided in [44] are used to develop a 5 DoF kinematic model of the human thumb as a 5-link serial chain. The thumb model is used for testing the thumb-exos kinematics during the design process and guide the obtained result to the fulfillment of the following requirements:

1. Not to constrain any of the 5 DoF of the thumb when the user is wearing the exoskeleton device.
2. To guide the opening and the closure of the thumb allowing a natural motion of the finger.
3. To provide the user with an effective transmission of the forces to the thumb phalanges.

4. To ensure the self-adaptability of the device to thumbs of different sizes.

5. To guarantee the possibility of integration with a hand-exos device grounded on the user's back of the hand.

5.2 Kinematics Features

The requirements for the new device define the guidelines followed for the design of the thumb kinematics. For the new thumb exoskeleton device a parallel spatial kinematics able to fulfill the mobility requirement is adopted, indeed the mechanical system composed by the human thumb wearing the exoskeleton has five non redundant DoF. Moreover, in order to have the possibility of guiding both the opening and the closure of the thumb allowing natural motions of the thumb itself, a kinematics with a high degree of underactuation is chosen for the new device. The thumb-exos is actuated by just one actuator; therefore the system maintains four degrees of freedom (DoF) mobility when the actuator is locked. These four degrees of freedom allow the thumb to perform a natural flexion-extension motion while guided by the actuation system in both the opening and closure motions.

Concerning the linear actuator, it has been inserted between an universal joint and a spherical joint in the kinematics in order to avoid the possibility of damage by a torque in any direction on the shaft.

The effectiveness of the force transmission between the exoskeleton and the thumb depends by the design of the connection interfaces. The elasticity, softness and mobility of the skin make difficult to effectively provide the thumb with longitudinal forces and torques by means of fasteners. Therefore the device is designed in order to apply only normal forces to the phalanges. In particular, the presented thumb-exos exerts two forces on the thumb, one force is applied on the 1^{st} Metacarpal phalanx whereas the second force is applied on the Distal phalanx. Referring to figure 29, the joints which connect the kinematics and the thumb phalanges are equivalent to a spherical joint superimposed to a prismatic joint oriented like the phalanx direction. In this way just a force normal to the phalanx's axis can be exerted on the finger by the thumb-exos. The loads are applied on the guides that are rigidly connected to the thumb phalanges by means of fasteners. Moreover, in both the connections, the prismatic joint parallel to the phalanx axis ensures the self-adaptability to phalanges with different lengths. Finally, in order to achieve the possibility of integration with a hand-exos device, the kinematic chain has been designed to be grounded on a link (ground-link) rigidly mounted on the back of the users hand.

5.3 Inverse Kinematics Solution

The thumb-exos kinematics has been designed based on a realistic thumb model. The thumb kinematic model has been realized by following the Denavit-Hartenberg (D-H) parameters presented in [44] and reported in table 4. Each group of four parameters (θ, d, a, α) allows to define the reference frame associated to each thumb joint by following the D-H convention. Referring to figure 30, the definition of the joint frames starts from Z_0, the ground reference attached to the trapezium, and it ends up to the Interphalangeal (IP) joint. In the table each joint has a tag depending on the kind of thumb motion it is responsible for, Adduction-abduction (AA) motion or Flexion-Extension (FE) motion. The D-H table defined in [44] has been used to develop a realistic CAD model of the thumb. Moreover the position of the thumb determined by the D-H table has been assumed as zero position for each joint. In the zero position the axes of the thumb phalanges are aligned.

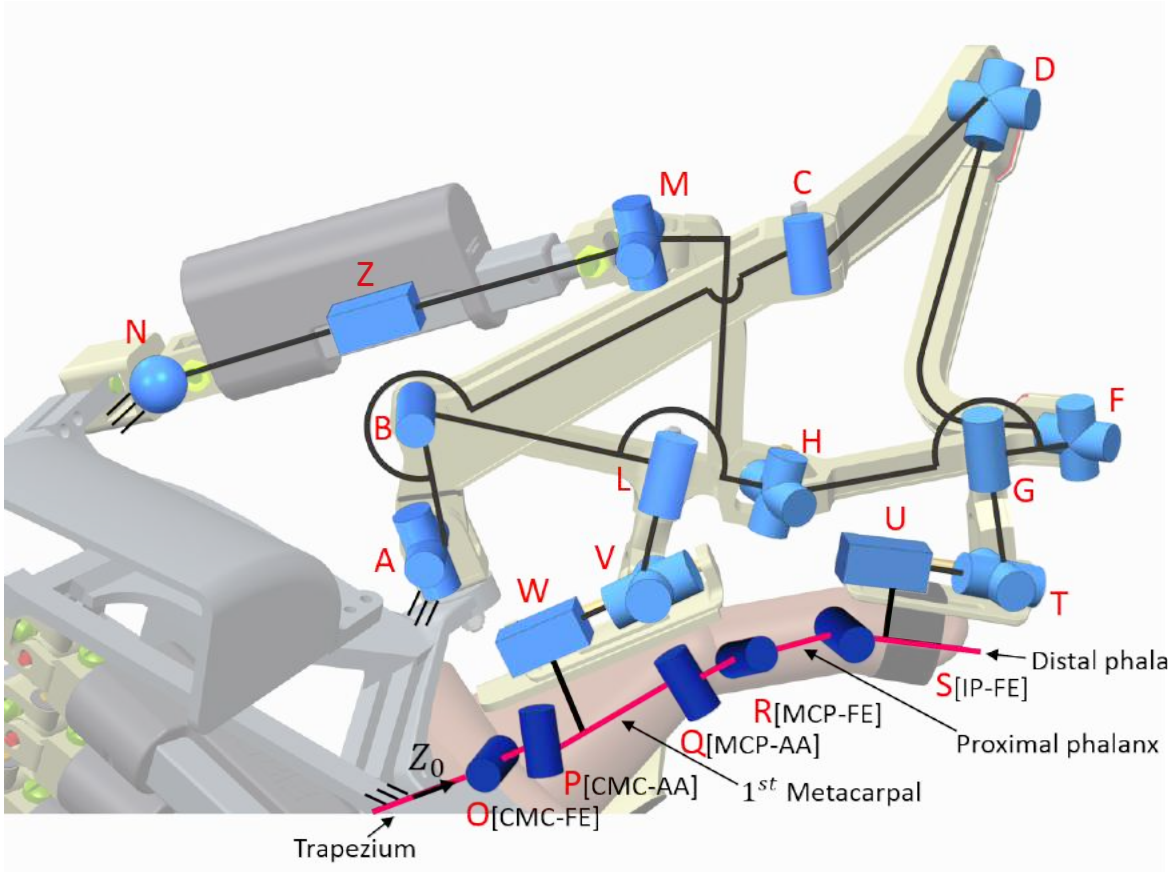

Figure 30: Schematic representation of the Thumb-exos kinematics attached to the thumb kinematics.

axis transition	θ	d	a	α
Z_0 to CMC(FE)	0	6.8	-1	-103.37
CMC(FE) to CMC(AA)	-92.57	-1	15.1	-69.59
CMC(AA) to MCP(AA)	28.89	15.4	35.6	-29.92
MCP(AA) to MCP(FE)	1.94	-18.9	10.3	100.93
MCP(FE) to IP(FE)	82.95	125.9	1	-21.63

Table 4: Denavit-Hartenberg parameters adopted to realize the thumb model. The values in table are part of the results of the study reported in [44].

The phalanges lengths has been experimentally measured among 15 healthy subjects aged between 25 and 43. The mean value of 50.1 mm has been found for the 1^{st} Metacarpal whereas 36.6 mm has been obtained for the length of the Proximal phalanx and 25.2 mm for the Distal phalanx.

The final scheme of the adopted kinematics for the realization of the thumb-exos is represented in figure 30. From the kinematic point of view the integrated system composed of the exoskeleton attached to the thumb is made up of six links (that belong to the exoskeleton) connected in parallel with the five links of the thumb model. Once defined the lengths of the links, the kinematic posture of the integrated system is completely defined by 5 joint coordinates (e.g. the pose of the thumb). The other 24 joint coordinates are determined by the solution of the

inverse kinematics. Since the device is underactuated, it is possible to control just one of the 29 joint coordinates of the integrated system, it is the prismatic joint. With its motion the prismatic joint guides both the opening and closure of the thumb.

In order to solve the inverse kinematics it is necessary to determine the spatial position and orientation of each joint of the mechanical system with respect to a ground coordinate system. A local reference frame has been associated to each joint according to the Denavit-Hartenberg convention and the homogeneous transformation matrix between each couple of successive joints has been determined. By composing the obtained homogeneous transformations four closed and independent loops through the joint frames have been determined. Referring to figure 30 the following independent loops have been defined:

$$ {}_{B}T^{C}\,{}_{C}T^{D}\,{}_{D}T^{F}\,{}_{F}T^{H}\,{}_{H}T^{B} = I \tag{15} $$

$$ {}_{A}T^{B}\,{}_{B}T^{M}\,{}_{M}T^{Z}\,{}_{Z}T^{N}\,{}_{N}T^{A} = I \tag{16} $$

$$ {}_{A}T^{O}\,{}_{O}T^{P}\,{}_{P}T^{W}\,{}_{W}T^{V}\,{}_{V}T^{L}\,{}_{L}T^{B}\,{}_{B}T^{A} = I \tag{17} $$

$$ {}_{A}T^{O}\,{}_{O}T^{P}\,{}_{P}T^{Q}\,{}_{Q}T^{R}\,{}_{R}T^{S}\,{}_{S}T^{U}\,{}_{U}T^{T}\,{}_{T}T^{G}\,{}_{G}T^{H}\,{}_{H}T^{B}\,{}_{B}T^{A} = I \tag{18} $$

where the generic ${}_{X}T^{Y}$ represents the homogeneous transformation matrix from the joint reference associated to the joint X to the joint reference associated to the joint Y. The independence of the loops is guaranteed by their definition. Indeed, every loop includes at least two successive joints which are not included in any of the other loops. Finally, by imposing the coincidence condition between the first and the last frame of each loop it is possible to determine 24 equations in the 24 unknown joint coordinates. The solution of the inverse kinematics has been used to numerically test the device for different poses of the thumb and solve the static of the system for each evaluated pose.

5.4 Statics Solution

As stated before the thumb-exos exerts two forces on the thumb phalanges, one on the Metacarpal phalanx and one on the Distal phalanx. Because of the high level of underactuation it is not possible to independently control neither the intensity nor their direction of the forces. In fact, the force direction and the ratio between the forces are defined by the kinematics features of the overall system composed by thumb and exoskeleton. In detail, the relation between the force exerted by the actuator and the forces exerted on the thumb is given by a Jacobian matrix of the system which depends by the link lengths of the structure and the pose of the assembled system. For a given pose of the thumb, once the inverse kinematics is numerically solved and the pose of the thumb-exos is determined, it is possible to write and solve the rigid body equilibrium equations for every link, neglecting the inertial forces. As result the torques at the thumb joints and the forces acting on the thumb phalanges are obtained.

In Section 5.5, the solution of the statics has been used within the link lengths determination process in order to evaluate the fitness of an individual that belongs to the population of the genetic algorithm.

5.5 Link Length Determination

The aim of this section is to describe the way the lengths of the links have been determined in order to improve the performance of the resulting thumb-exos kinematics. The 14 lengths which determine the link shapes represented in figure 32 have been optimized by means of a genetic algorithm. The fitness function has been defined in order to obtain the following results:

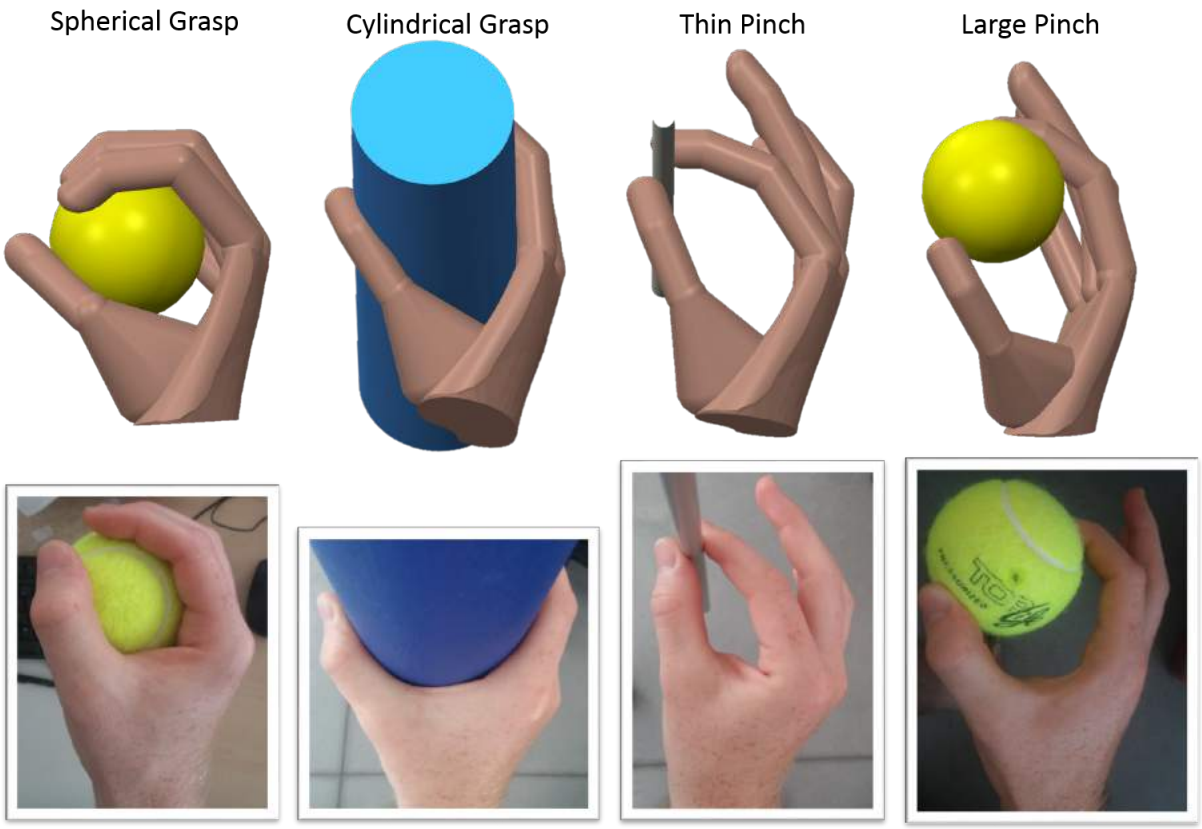

Figure 31

- maximize the sum of the forces exerted on the thumb phalanges by the exoskeleton;
- minimize the difference between the two forces;

The starting values for the lengths have been determined by the first non-optimized solution, that was experimentally obtained with a CAD software. These values are listed in the left column of table 6. The optimization search space has been limited by assuming as lower limits 0.5*(starting lengths) and as upper limits 1.5*(starting lengths). These limits have been chosen in order to look for solutions in a reasonably wide search space limiting the lengths combinations that lead to a too much different kinematics or mechanically unfeasible kinematics that numerically show better performances.

The performance of the system has been evaluated on the open hand pose plus four common grasping poses. The coordinates of the thumb joints for each of the five poses have been determined by visually comparing the thumb CAD model defined in Section 5.3 with the pictures of a hand performing the four grasping poses (figure 31). Referring to figure 31 the thumb kinematics has been optimized in the following grasping poses: *spherical grasp* , *large pinch* , *cylindrical grasp*, *thin pinch* and the *open hand* pose.

With respect to the zero position the joint angles of the thumb joints are listed in table 5 for each grasping pose.

As previously mentioned, the optimization has been performed by means of a genetic algorithm. The designed genetic algorithm works with a population of 100 individuals. Moreover, a stall generation limit is adopted as convergence criteria. In detail, the algorithm is programmed to stop when the cumulative change in the fitness function value over 10 generations is less than 0.0001.

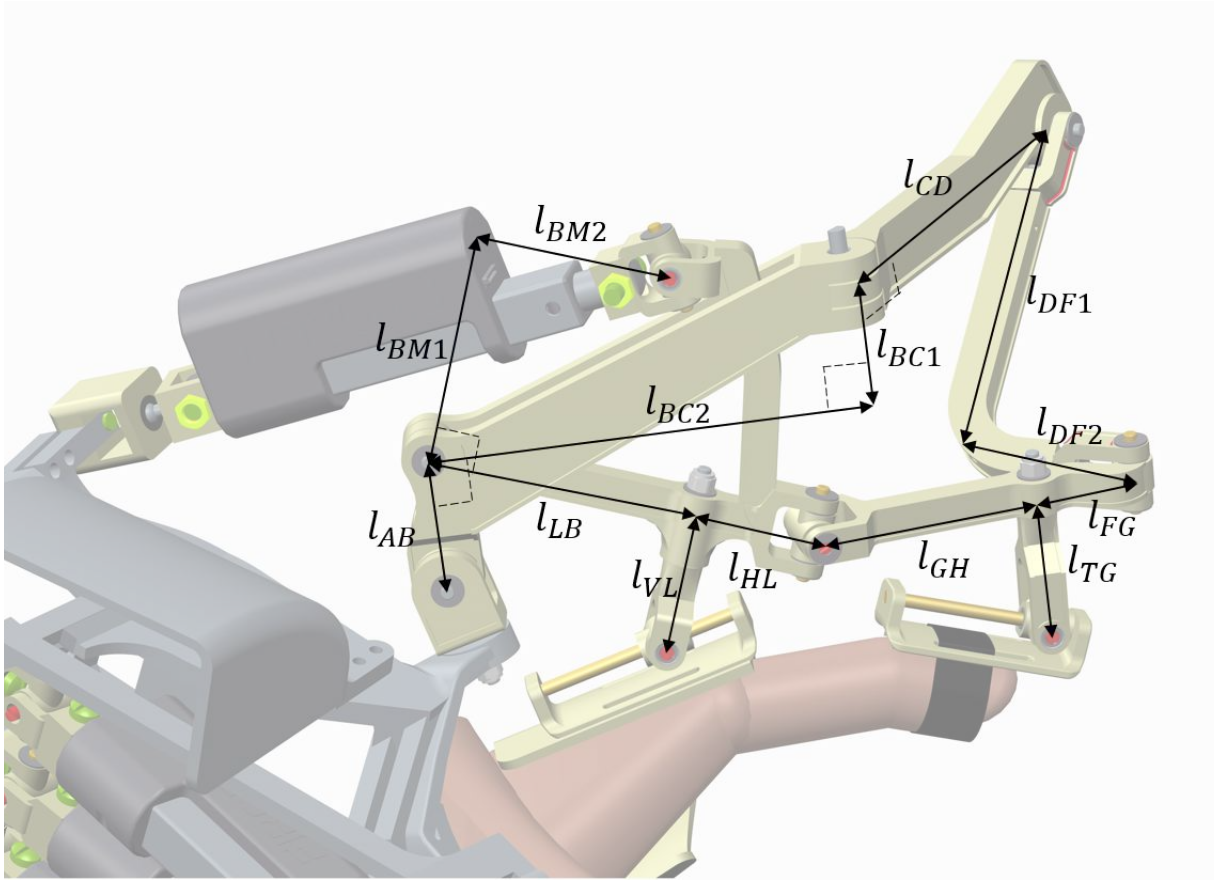

Figure 32: Representation of the optimized lengths of the Thumb-exos device.

Pose	CMC (FE)	CMC (AA)	MCP (AA)	MCP (FE)	IP (FE)
open hand	-10	10	-1.37	32.13	12.7
spherical grasp	34.46	-37.22	7.7	38.27	37.77
cylindrical grasp	20	-30	-5	5	45
large pinch	10	-28.32	1	15	30
thin pinch	35	-22	-5	10	30

Table 5: Thumb joint angles for the five grasping poses with respect to the zero position expressed with the D-H table.

The adopted GA fitness function (FF) is shown in equation 19. It is defined as the mean of a performance parameter (PP) evaluated over the five testing poses.

$$FF = \frac{\sum_{i=1}^{5} PP_i}{5} \tag{19}$$

$$PP_i = \frac{1}{|\vec{F_i}| + |\vec{f_i}|} + W_1 \frac{|\vec{F_i}|}{|\vec{f_i}|} + W_2 P_i \tag{20}$$

Equation (20) shows how the performance parameter (PP) is defined. Referring to equation (20), PP_i is the performance parameter evaluated for the i^{th} grasping pose, F_i and f_i are respectively the major and the minor force exerted on the thumb phalanges and evaluated by solving

label	starting length [mm]	min. search space [mm]	max. search space [mm]	optim. length [mm]
l_{AB}	35	17.5	52.5	30.24
l_{BM1}	49.4	24.7	74.1	52.87
l_{BM2}	32.7	16.35	49.05	42.44
l_{BC2}	72.5	36.25	108.75	95.33
l_{BC1}	45.5	22.75	68.25	25.79
l_{CD}	140	70	210	102.46
l_{DF2}	77	38.5	115.5	40.98
l_{DF1}	57	28.5	85.5	82.51
l_{FG}	29.8	14.9	44.7	22.12
l_{GH}	55.1	27.55	82.65	51.13
l_{HL}	35	17.5	52.5	26.31
l_{LB}	60	30	90	59.77
l_{VL}	21.5	10.75	32.25	31.45
l_{TE}	34.5	17.25	51.75	31.59

Table 6: Starting lengths used to run the optimization GA process (left column), GA search space limits and optimized lengths obtained as output of the genetic algorithm (right column).

the statics of the system. W_1 and W_2 are two arbitrary weights assumed experimentally for this optimization as 10 and 5 respectively. Finally, P_i is a penalty value. The PP is the sum of three components. The first component is the inverse of the sum of the two forces exerted by the exoskeleton on the thumb, whereas the second component is proportional to their ratio and by definition is always greater than one. The last component is proportional to the penalty value. The penalty value P_i is non-zero when at least one of the three prismatic joint coordinates is out of its admissible range. Every time the inverse kinematics is solved for a population individual within the genetic algorithm and the PP_i is evaluated for each of the testing poses, the penalty value assigned to that individual is the sum of the absolute values of the possible overshoots of each of the three prismatic joints of the kinematics with respect to their limits. The admissible ranges for the prismatic joint coordinates have been assumed as:

- 0-60 mm for the slider on the metacarpal phalanx
- 0-40 mm for the slider on the distal phalanx,
- 123-173 mm for the actuated prismatic joint.

The difference between the limits assumed for the actuated prismatic joint represents the maximal stroke of the adopted linear actuator, which is 50 mm. In table 6, the obtained optimized lengths are listed in the right column. The results of the optimization has been reported in the right column, whereas the starting guess in the left column. It is possible to notice that none of the optimized lengths is on the boundary of the search space. The fitness function obtained with the optimized lengths significantly improved. Indeed, $FF_{start} = 50.6363$ is the fitness function value obtained by the thumb-exos kinematics evaluated with the starting link lengths, whereas after the optimization the value $FF_{optim} = 24.07$ is obtained. Concerning the effect of

Pose	Starting Solution		Optimized Solution	
	$F1$	$F2$	F1	F2
open hand	0.83	0.28	0.47	0.48
spherical grasp	0.89	0.23	0.38	0.38
cylindrical grasp	1.64	0.26	0.54	0.35
large pinch	1.26	0.21	0.38	0.39
thin pinch	1.26	0.26	0.41	0.32

Table 7: Force values evaluated by adopting the starting lengths and adopting the optimized lengths. Forces are calculated for a unitary actuation force.

the optimization on both the forces exerted by the exoskeleton on the two phalanges. In table 7, the force values obtained with a unitary actuation force are listed for each pose evaluated. The values are reported for both the kinematics defined by the starting link lengths and the optimized kinematics. It is possible to notice that in the optimized solution the obtained force values are similar among the five grasping poses, moreover, for each pose, F1 is similar to F2 as expected.

5.6 Thumb-Exos Structural Design

Figure 33: The thumb-exos prototype.

Figure 33 shows the realized prototype of the thumb exoskeleton designed. In order to reduce the total weight of the device, the links are designed in order to be printed in light

material by means of a rapid prototyping 3D printer. Moreover, in order to improve the comfort and the wearability, the entire ground link has been modeled over a 3D reconstruction of a real hand acquired with an RGB-D Kinect camera. In this way an ergonomic shape for the contact surface has been obtained leading to a more natural contact between the interface and the back of the user's hand. A layer of foam on this surface will improve the adaptability to different hand sizes and the adherence between the device and the back of the hand. All the joints but the spherical are realized by custom aluminum pins coupled with low friction plastic bushings in order to reduce the friction load on the thumb while it is moving. The spherical joint at the base of the actuator and the actuator itself are commercial component integrated in the kinematics design process. A Firgelli P16 linear actuator (DC motor with screw mechanism, 50N stall output force, 50 mm stroke) was chosen to actuate the thumb, and was coupled with a miniaturized strain-gauge 1 DoF force sensor (SMD Sensors S215, 55 N full scale) mounted at the base of the actuator. Concerning the transmission of the forces to the thumb, because of the perpendicularity between the forces transmitted and the phalanx axes, the fasteners don't need to be excessively tight around the finger to effectively load the thumbs phalanges and not to move from the starting position. This kinematic feature allows to improve the level of comfort perceived by the user while he is wearing the device. Referring to figure 33 it is possible to notice that the fasteners are composed by a rigid 3D printed part kept in position by one or more fabric stripes. In particular, one stripe is used to keep the thimble attached to the distal phalanx, whereas two fabric stripes are used to keep the ergonomic plastic part attached to the 1^{st} metacarpal, one stripe is wrapped around the phalanx close to the joints and the other is wrapped around the wrist.

5.7 Experimental Methods

Two different experimental sessions have been conducted in order to evaluate the developed mechanism for the thumb exoskeleton: the first aimed to qualitatively evaluate functionality of the exoskeleton in grasping objects of different shape and size. The second experiment involved different hand sizes and made used of position, force, pressure and EMG sensors in order to investigate propagation of forces during a grasping and releasing sequence of operation. In the first experiment one healthy subject (male, age 28) wore the whole hand exoskeleton, composed of the finger mechanisms presented in [45] and of the here proposed mechanism for the thumb. The subject was seated in front of a desk and the exoskeleton was held by a fixed support. Due to the non-backdrivability of the actuators, a simple force control was implemented to operate the device. The algorithm closed a control loop between the reference voltage supplied to each DC linear actuator and each strain gauge force sensor mounted between the actuator and the chassis of the exoskeleton. The control algorithm was executed at 250 Hz on a Beagleboard microcontroller board and Texas Instruments DRV8835 H-bridge ICs were used to drive the actuators. The control loop enabled the user to actively move the fingers and the exoskeleton in transparency and to test finger closure on different objects. A tennis ball (diameter 70 mm), a plastic cylinder (diameter 80 mm) and a metal cylinder (diameter 10 mm) were used in the evaluation. The second experimental session investigated forces applied by the exoskeleton in grasping and releasing tasks with different hand sizes. In this experiment, a pressure sensorized water bottle (presented in [28]) was used to measure the overall pressure exerted by the hand during grasping. A miniaturized optical force sensor (OptoForce OMD-10-SE-10N, range 10 N, resolution 1 mN) was implemented to measure contact forces between the thumb and the object. The strain gauge sensor at the base of the actuator and the linear potentiometer integrated inside the actuator provided also information about force and displacement applied

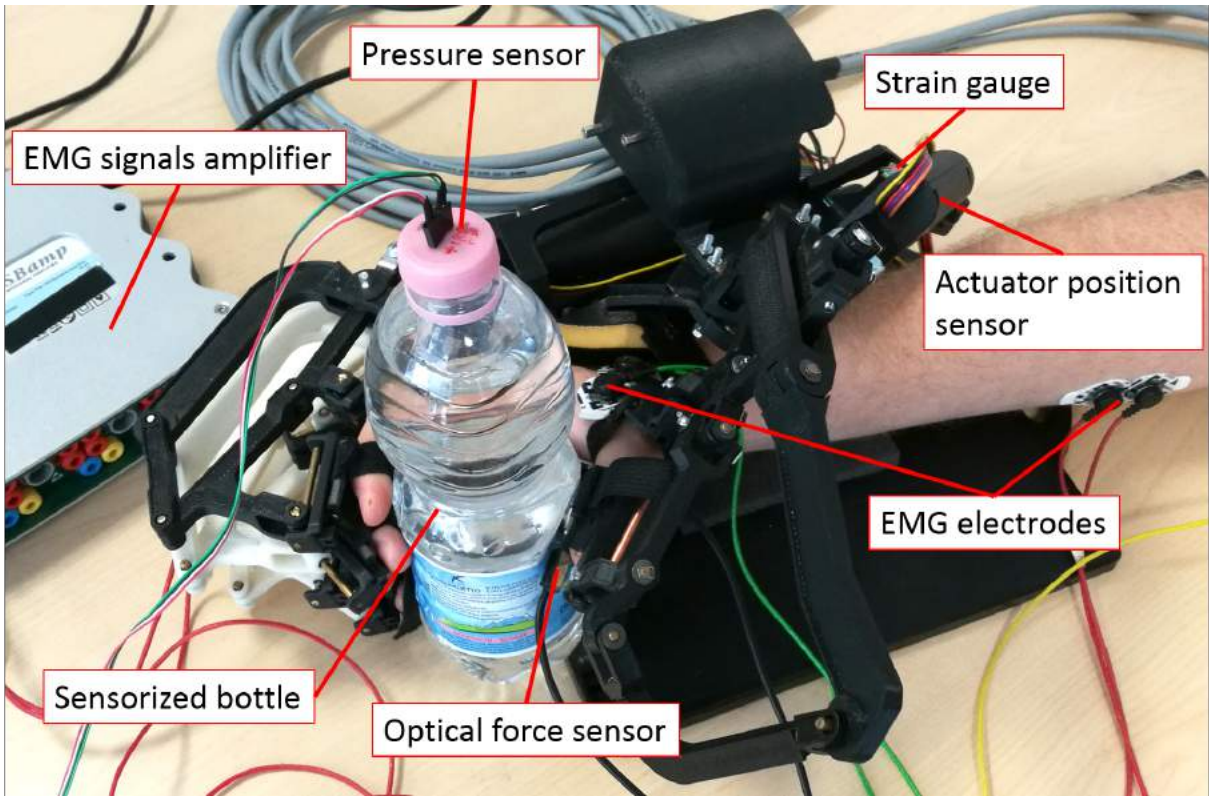

Figure 34: The experimental setup.

at the actuator level. Additionally, EMG signals were acquired in bipolar configuration in proximity of the Adductor Pollicis muscle, in order to monitor muscle relaxation during the active exoskeleton operation. Similarly to the previous experiment, subjects wore the whole hand exoskeleton. They were seated in front of a desk and the exoskeleton was held by a support (Figure 34). A preliminary experimental phase was conducted with one healthy subject (male, age 28), and evaluated forces exerted by muscles during a natural and stable grasping of the sensorized object. In this phase the exoskeleton was controlled in transparency modality similarly to the previous experiment) and the subject was asked to actively grasp and release the sensorized object ten times. He was asked to apply the amount of force he felt comfortable for a stable grasping. The exerted maximum contact force was then used to tune the reference voltage fed to the thumb actuator for the next experimental phase. In the final experimental phase, the subject's hand was held completely passive and the actuator actively assisted the closing and opening of the thumb. Three healthy subjects participated to the experiment (male, aged 29 ± 2) with different hand sizes as reported in Table 8. A feed-forward reference voltage was fed to the actuator, shaped as shown in figure 37, in order to slowly close and open the thumb. The sequence was repeated ten times for each subject. Subjects were asked to keep the hand completely relaxed and the rectified and filtered EMG signal was monitored to be below 30 uV throughout the closing phase (according to results measured in the preliminary experimental phase).

5.8 Experimental Results

Regarding the first experimental session, involving grasping of objects with different size and shape, a stable grasping was achieved with all the tested objects as shown in Figure 35. Fingers and the thumb mechanism could adapt to the object surface and each object was held lifted

	Subject 1 [cm]	Subject 2 [cm]	Subject 3 [cm]
Hand size	17.5	18	21.5
Thumb size	9.7	10	11.5

Table 8: Subjects hand size was measured from the center of the wrist to the top of the middle finger on the palm side with the finger completely extended. The thumb size was measured on the back hand side from the 1^{st} metacarpal base to the top of the thumb when it is aligned to the forearm.

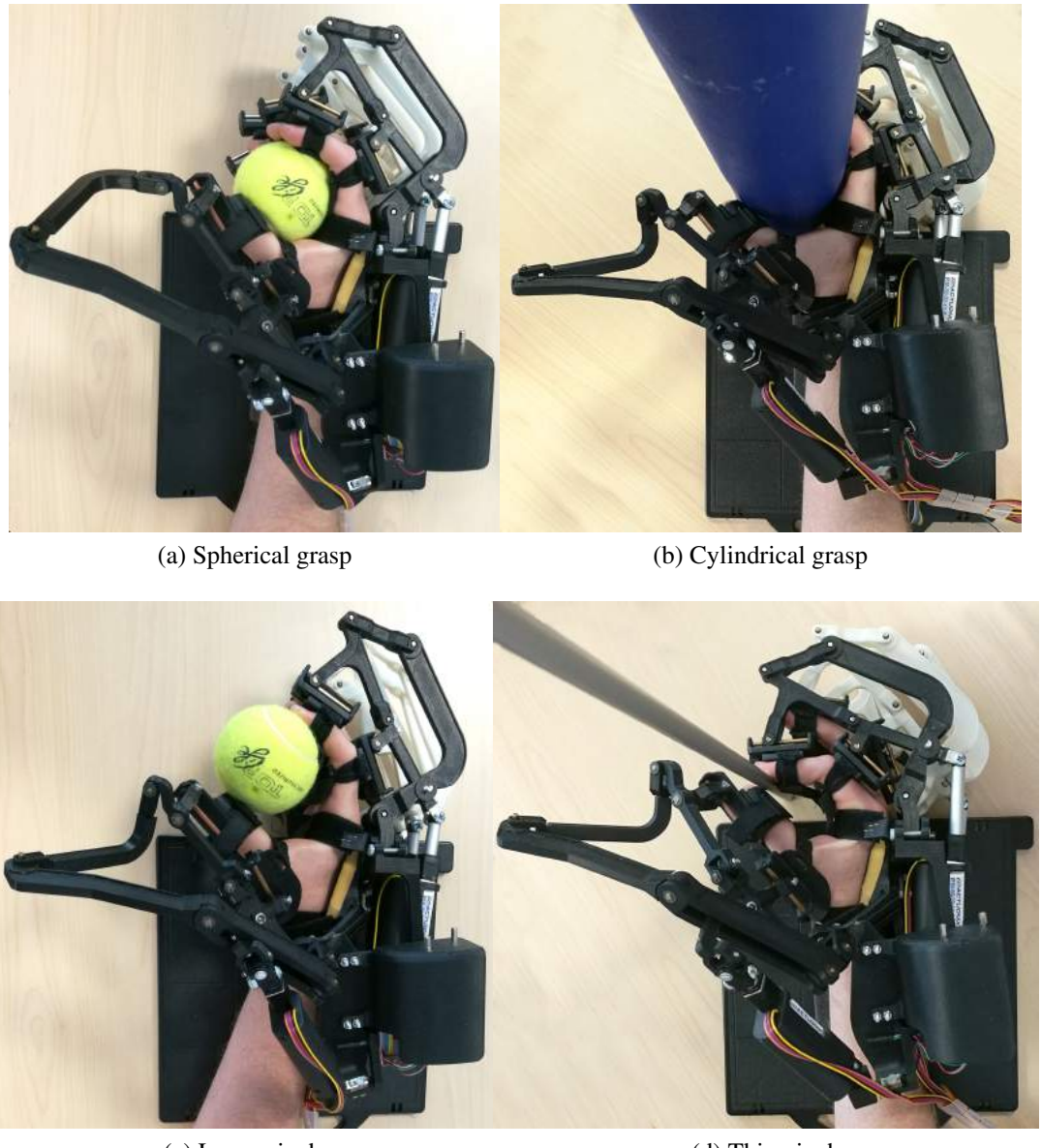

(a) Spherical grasp

(b) Cylindrical grasp

(c) Large pinch

(d) Thin pinch

Figure 35: Hand grasping tests

off the surface of the table. Although the grasping was actively driven by the subjects and the exoskeleton did not provide any guidance or assistance to the grasping, it shows the proposed mechanism could adapt to objects of different shape and size. Regarding the preliminary phase

of the second experiment, a feed-forward voltage profile, reported in Figure 37 was obtained for driving the actuator in order to match, in the robotic driven modality, the contact force measured during the muscle-driven grasping and opening sequence. Since the actuator was fed with the same feed-forward reference voltage profile, at stall the estimated output force of the actuator was the same for all repetitions. Graph in Figure 36b show similar maximum contact forces, averaged over ten repetitions, for both the muscle driven and robotic driven modalities (maximum measured contact force: 3.68 N muscle driven, 3.11 N for the robotic driven). Regarding the recorded muscle activity, graph in Figure 36a show noticeable activation of the Adductor Pollicis during the grasping phase of the muscle driven modality (40 uV) with respect to the relaxed hand of the robotic driven modality (25 uV). EMG signals were rectified and filtered (low-pass filter, 3 Hz cut-off frequency). Also, in the robotic driven modality EMG activity is at minimum during the grasping phase but conversely slightly increases during the opening phase (32 uV). This might be caused by residual resistance opposed by muscles during the full robotic-driven opening of the thumb. Regarding results of the second experimental phase, for all the three subjects the thumb mechanism was able to assist a complete grasping and opening sequence with similar behaviour, as shown in graphs of Figure 38. In particular the graph related to position of the linear actuator in Figure 38a shows a transient period corresponding to the thumb going in contact and pressing the sensorized object. After the initial transient period, the position of the linear actuator stabilizes for all the subjects to different linear dimensions, corresponding both to different deformations of the grasped object and different configurations of the thumb mechanism. Estimated output force of the linear actuator was in line with measurement of the strain gauge force sensor mounted at the base of the actuator, as shown in Figure 38b. Regarding the measured contact force and the overall pressure exerted on the grasped object, output values depended also on the different thumb dimensions, resulting in different configurations of the thumb mechanism and different propagation of forces. Yet, the profile of the contact force was comparable between subjects (Figure 38c), with a maximum relative difference of 19.8% (between Subject 2 and Subject 3) of the maximum contact force. Subject 3 measured the lowest contact force and corresponded to the subject with the higher hand size. Regarding the overall grasping pressure shown in Figure 38d, differences were more evident resulting in a relative difference of 43% (between Subject 3 and 1) of the maximum measured pressure. Also it has to be noted that Subject 1 reported a relatively different pressure profile with respect to subject 2, although hand size and thumb size were similar. This relatively small difference might be explained by the complex thumb kinematics and stiffness of the human hand that might show differences not completely caught by the length of the segments only.

6 Pedals

The CENTAURO robot is conceived for being driven using a pedals platform as a control navigation station. The CENTAURO robot can move exploiting the 3-DoF in the plane: I) moving forward and backward; II) rotating; III) left and right horizontal translations.

Basic Idea In order to cover this relatively high number of DoF with a single pedal platform and keep the navigation control strategy simple and intuitive, the rudder pedals solution used also as a part of the primary cockpit flight controls has been exploited. In particular, the rudder pedals (show in Figure 39) consist of two unidirectional pedals linked through a sensorized bar. In this way the user is allowed to press independently the unidirectional pedals and, in the meantime, to move the rudder bar left or right. Thus, in the control scenario we envisaged,

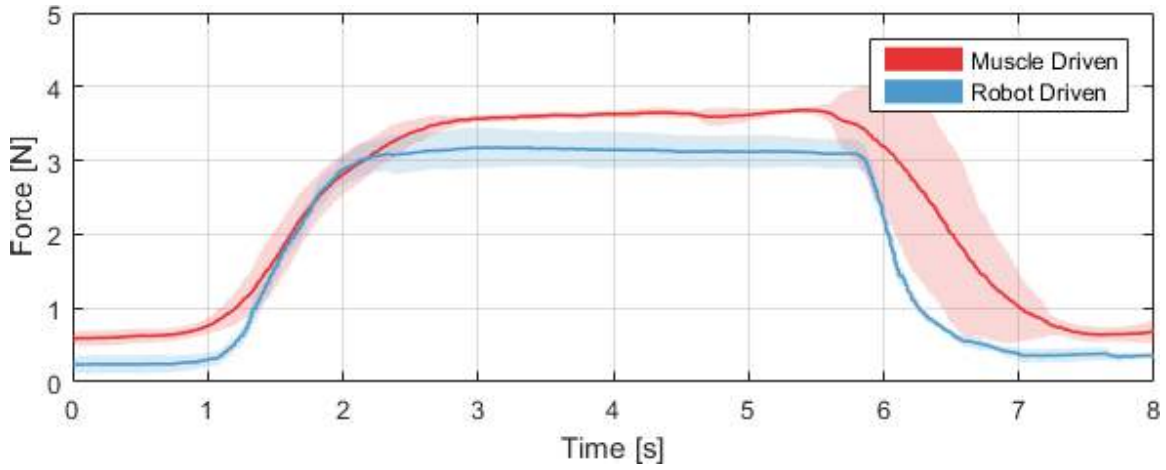

(a)

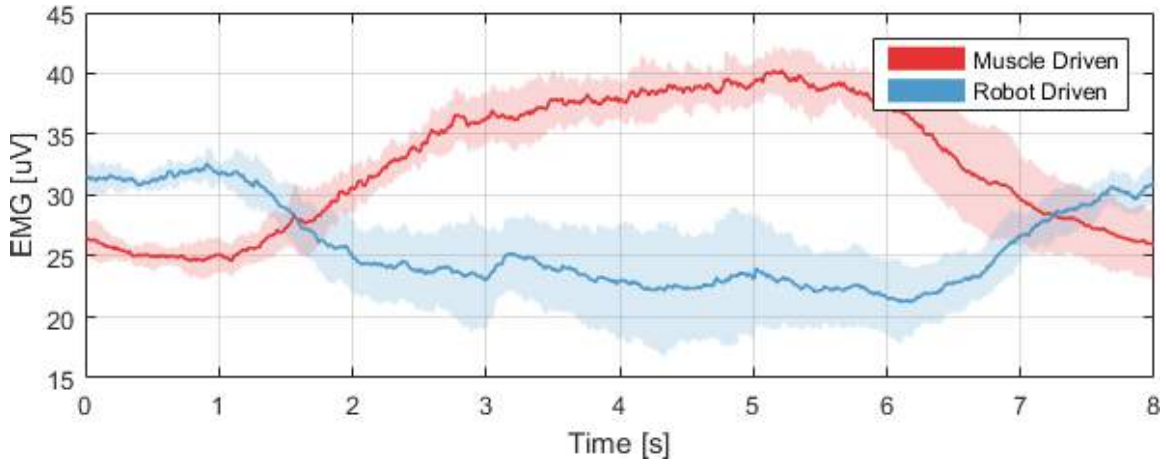

(b)

Figure 36: Measured thumb contact force (top) and rectified and filtered EMG signals (bottom) of the Adductor Pollicis during the active (Muscle Driven) and passive (Robotic Driven) closing of the thumb, averaged over ten repetitions

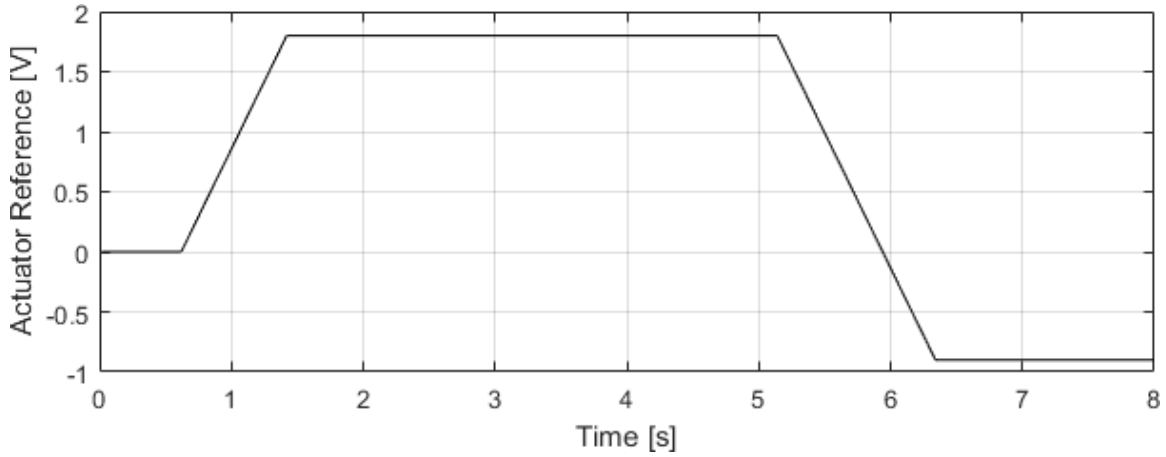

Figure 37: Reference voltage fed to the thumb actuator in order to actuate the closing and opening sequence

the right and left unidirectional pedals are used for moving the robot forward and backward

Table 9: Control Strategy. For each task is reported the positions of the three potentiometer (rudder, left pedal and right pedal). The last two tasks refer to the horizontally translations and the double "'+"' sign indicates that both pedals have to be pressed more than half of their maximum range

TASK	RUDDER	LEFT	RIGTH
No move	0	0	0
Moving Forward	0	0	+
Backward	0	+	0
Turn Right	+	0	0
Turn Left	-	0	0
Step Right	+	++	++
Step Left	-	++	++

respectively (positive and negative speed along the direction the robot is facing at) and the rudder bar is using for turning right and left (right foot forward and left foot backward will left rotate the robot for instance). Furthermore, the user can also translating horizontally by pressing both pedals simultaneously and then rotating the rudder left or right dependently on the desired direction.

Hardware and software Implementation A commercially available flight rudder pedal simulator has been adapted for being the pedal platform of the CENTAURO robot (ThrustMaster® T.Flight Rudder Pedals). Instead of using the proprietary software for reading the three potentiometers (2 for the pedals and 1 for the rudder) an Arduino board ("'Genuino Uno"') has been used for the ADC conversion coupled with an Arduino Ethernet Shield for enabling the UDP communication. The hardware setup is shown in Figure 40.

The three signals are conditioned internally to the Arduino microcontroller in a way that: each pedal is 0 when not pressed and the rudder is positive and negative when turning right and left respectively (0 in the central position). The control strategy, already tested in a simple XVR custom made space-ship like game, is reported in Table 9.

As stated above, the implemented control strategy allows the user to move back and forward by pressing left and right pedal respectively and to turn left and right by moving the rudder with the right and left foot forward respectively. Furthermore, the simultaneous pressure of both pedals more than half of their ranges, allows the user to control the horizontal translations.

7 Bilateral Teleoperation with Alex

This section presents the implementation of the Time Domain Passivity Approach-based controller with the Alex exoskeleton as master device. The teleoperation architecture is basically a Position-Force (measured) schema with Position Drift compensation. The teleoperation architecture has been tested in the Cartesian Space performing high-force stiff contacts in different directions in the Cartesian space under communication delays, even including multi-directional contacts.

7.1 Control Architecture

Since the remote manipulation tasks are defined in the Cartesian space, master and slave share the information regarding the three translational DoFs at the end-effector level: positions, velocities and forces. For this reason, the time domain passivity theory (see Sections 6.2 and 6.3 in Deliverable D3.2) has been implemented for each of the three DoFs, independently.

7.2 Experiments

The experiments were carried out to investigate the performance of the position-force (measured) TDPA schema when the involved robots are mechanically different. The experimental setup was composed of the two exoskeletons, one acting as master (Alex Exoskeleton, Figure 43) and the other as slave device (Rehab Exoskeleton, Fig. 44), and a solid structure used to perform high-stiffness contacts along three surfaces, one for each Cartesian axis. A picture of the system setup is shown in Fig. 45.

Regarding the master device, the local control is an open-loop force control. In detail, the master controller applies the desired torques (obtained from the slave measured forces) plus the gravity, the static friction and the viscous compensations acting as a haptic interface. The slave device implements a closed-loop position control, i.e. a PD control with a gravity and dynamic compensation. Dynamic compensation is due to an acceleration observer that use both joint torque sensor and encoder position reads. The proportional and derivative gains of the slave position control have been chosen such that the position error at the end-effector (when no forces are applied at the end-effector) is less than $0.5\ mm$ with a maximum speed of $0.5\ m/s$.

The gains used in these experiments are reported in the Tab. 10. Both the master and the

Table 10: The proportional and derivative gains used for the 4 joint slave position controls.

Joint	K_p **[**Nm/rad**]**	K_d **[**$Nm \cdot s/rad$**]**
J1	4000	40
J2	3000	40
J3	3000	50
J4	5000	35

slave systems ran with a time step of $200\ \mu s$, while the communication loop-back was less than $1\ ms$ when no time delay was introduced.

The bilateral teleoperation system was initially tested without communication delay, both in free movement and in contact with the rigid environment, i.e. the rigid solid body. In these two conditions, the overall system exhibited a stable behavior without the necessity of the passivity controller.

The conducted experiments was develop to explore how the TDPA works in rescue operation like situation, thus an high delay value was chosen. The simulated communication delay was set to $40\ ms$ in both sending and receiving, i.e. $80\ ms$ round-trip.

The experiments were articulated in three different tests:

- Contact with flat surfaces in the three Cartesian axes (each individually), with delay and the Passivity Controller on;

- Contact with flat surfaces in the three Cartesian axes (each individually), with delay and the Passivity Controller off;
- Contact with a sharp corner (two or three Cartesian axes involved), with delay and the Passivity Controller on.

In all the experiments the user drove the slave robot closed to the stiff surface and tried to push the slave end-effector against it. The user tried to hold the contact between the surface and the slave robot as long as possible when the passivity controller was off.

7.3 Results and Discussion

This section presents and discusses the results of the set of tests described in the previous section. The main results of the conducted experiments are reported in the next four figures (Figs. 46,47,48 and 49) that share the following notation for the Cartesian space signals: p_m^x, p_m^y, p_m^z indicate the three components of the master EE position; p_s^x, p_s^y, p_s^z refer to the three components of the slave EE position; p_{sd}^x, p_{sd}^y, p_{sd}^z refer to the three components of the slave EE reference position; f_e^x, f_e^y, f_e^z indicate the three components of the interaction force between the slave EE and the environment; f_{md}^x, f_{md}^y, f_{md}^z indicate the three components of the reference force at the master EE; finally, $e_p^{x,y,z} = p_m^{x,y,z} - p_s^{x,y,z}$ are the position errors between the master and slave EE.

The figures Fig.46, Fig.47 and Fig.48 report the data acquired when the teleoperator system has been evaluated exerting force along only one direction at the time (X, Y and Z, respectively). Focusing on the left part of the three figures, that shows the data acquired when the passivity observer was OFF, it is easy to observe the unstable behavior of the whole teleoperator system. In these cases, independently of the involved axis, the subject operating with the master device has not been able to perform a stable contact with the remote stiff wall. The extra energy generation due to the communication delay causes force bursts at the master side that impede a stable contact between the slave EE and the environment. This behavior can be analyzed looking at both the oscillatory trend of master and slave position components and the force bursts at the slave side that are back propagated to the master side. Focusing, instead, on the right part of the three figures, that shows the data acquired when the passivity observer was ON, the reader can perceive the stability of the overall teleoperator system. The extra energy dissipation at the both sides, thanks to the two passivity controllers, allows the operating subject to perform a remotely stable contact along each of the three axes. Hence, the effect is that the operator can modulate as he prefers the duration of the contact and the module of the force applied to the environment. The stability can be observed by looking at the position errors that are less jerky when the passivity controller is enabled.

It is also worth noting that the slave position drifts respect to the master position when the passivity controller is enabled. In fact, it is important to remember that the position drift compensator becomes active only when the slave is not passive. As example, the reader can notice the drift during most of the X-axis contact duration in Fig.46 (from 1.5s to 6s), during the first contact along the Y-Axis in Fig.47 (from 1.5s to 3s) and, in the case of the Z-axis, both during the contact (from 1.5s to 2.2s) and during the free movement (from 3.5s to 8s). As explained above, when the slave is not passive extra energy can be injected to the slave for compensating the position drift; this effect can be seen at t=6.5s in Fig.46, at t=3s in Fig.47 and at t=2.2s and t=8.3s in Fig.48.

As described in the experiment part, the teleoperator system has also been evaluated in multi-axes contacts. The operators were asked to push against a corner exerting hence a force

having at least two main components. As example, the results of the corner experiment involving the X and Y axes are shown in Fig.49. All the considerations discussed above can be applied to this practical case. The passivity controller intervenes during the contact with the corner stabilizing the interaction, avoiding a bounce effect between the two sides of the corner.

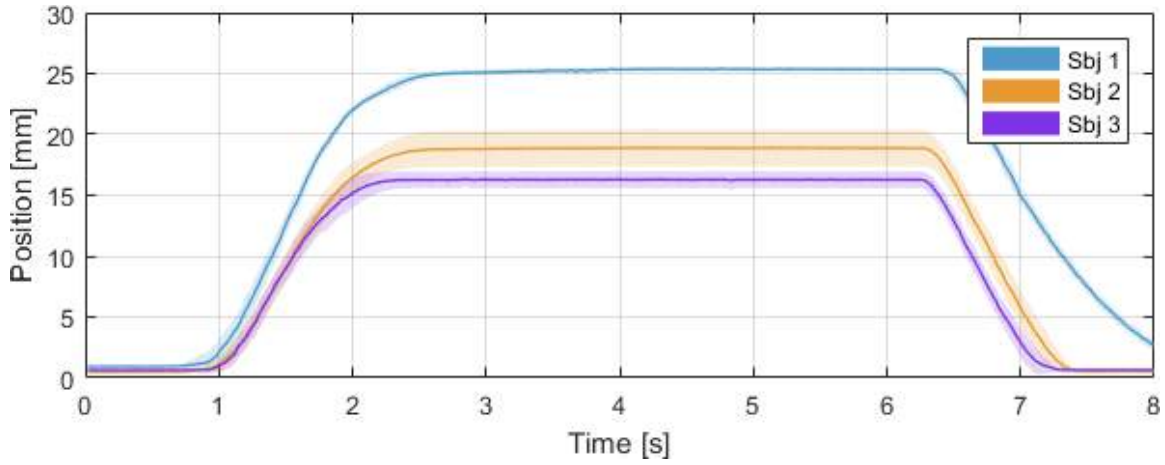
Position [mm]
Time [s]
Sbj 1
Sbj 2
Sbj 3

(a)

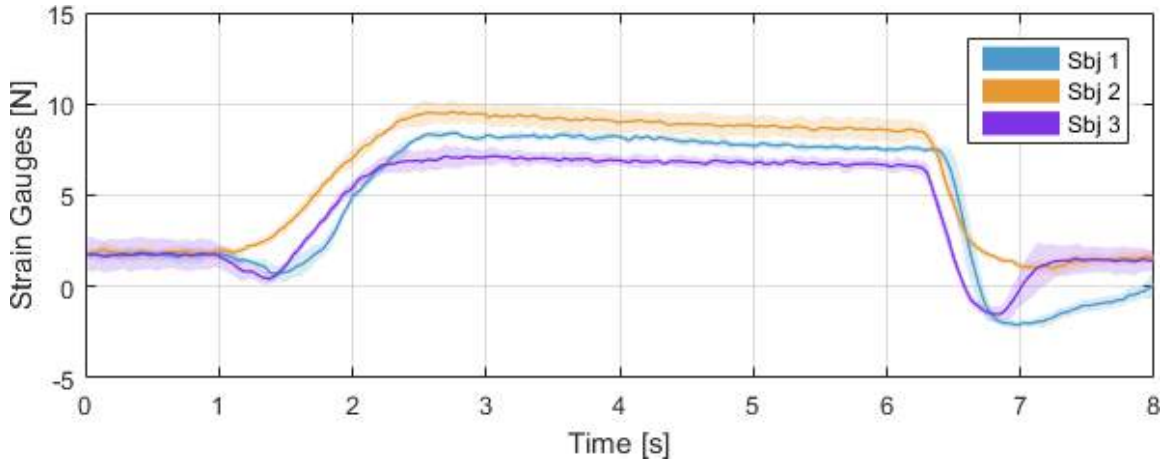
Strain Gauges [N]
Time [s]
Sbj 1
Sbj 2
Sbj 3

(b)

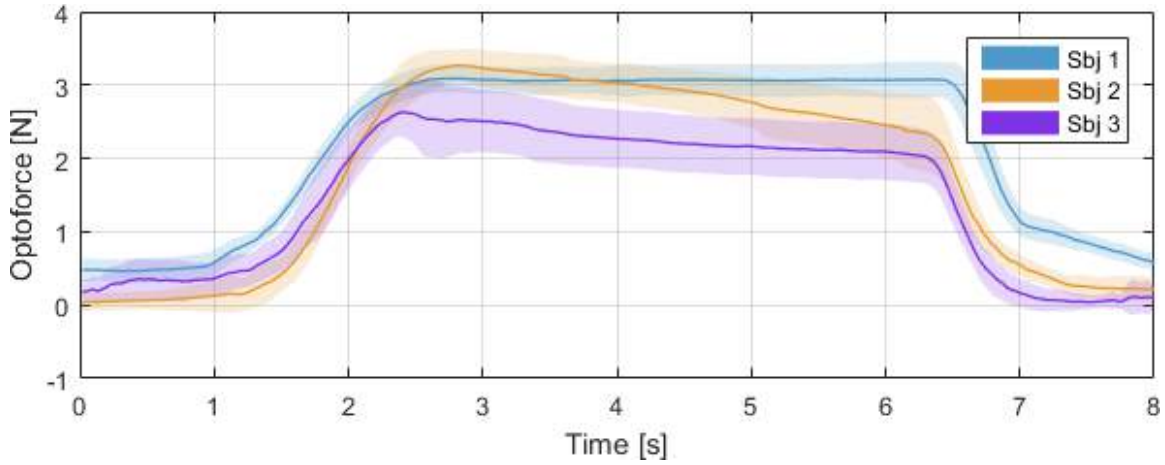
Optoforce [N]
Time [s]
Sbj 1
Sbj 2
Sbj 3

(c)

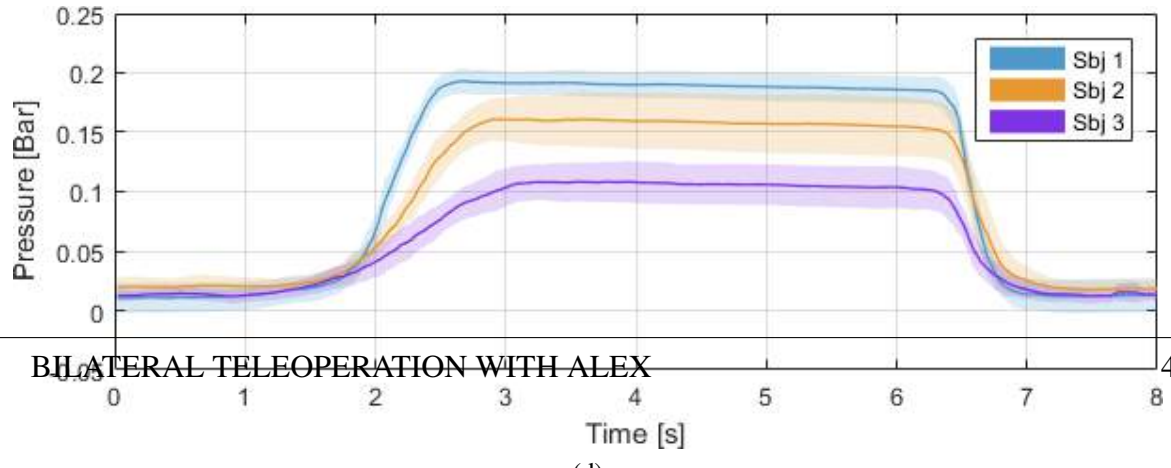
Pressure [Bar]
Time [s]
Sbj 1
Sbj 2
Sbj 3

(d)

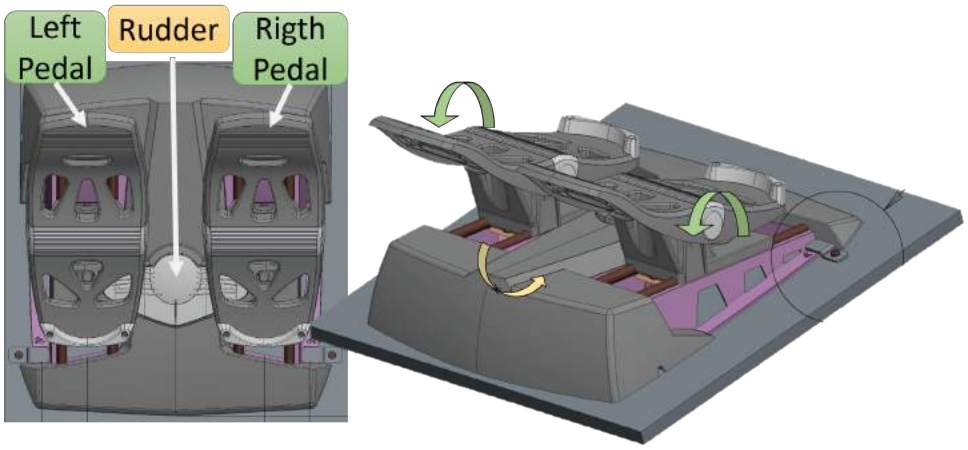

Figure 39: Overview of the rudder pedals platform

Figure 40: Hardware setup. The output of the three potentiometers of the rudder pedals have been attached to the Arduino board for the ADC conversion and the UDP communication.

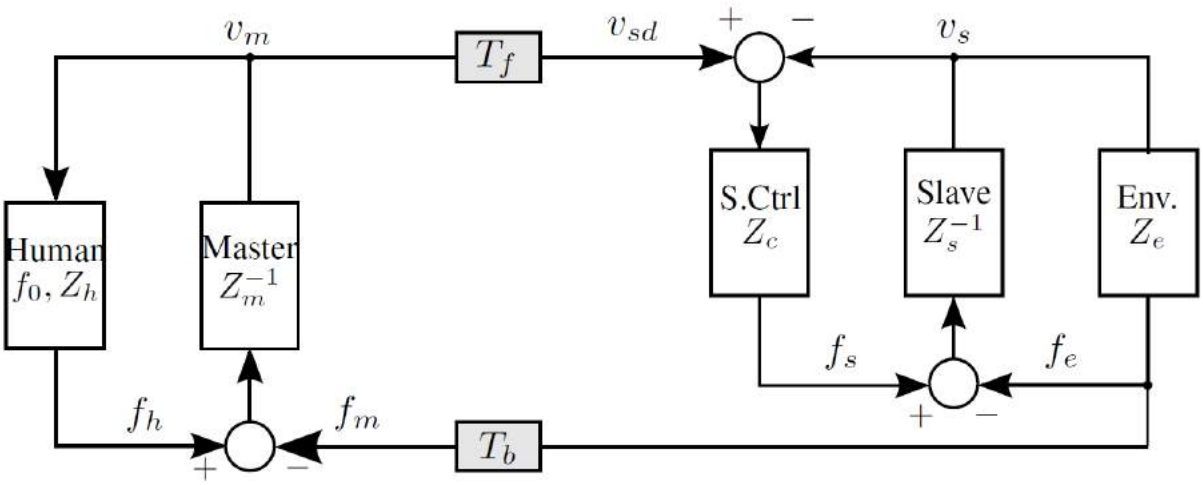

Figure 41: The block diagram of the P-F(measured) Teleoperation Architecture. Contribution from [3].

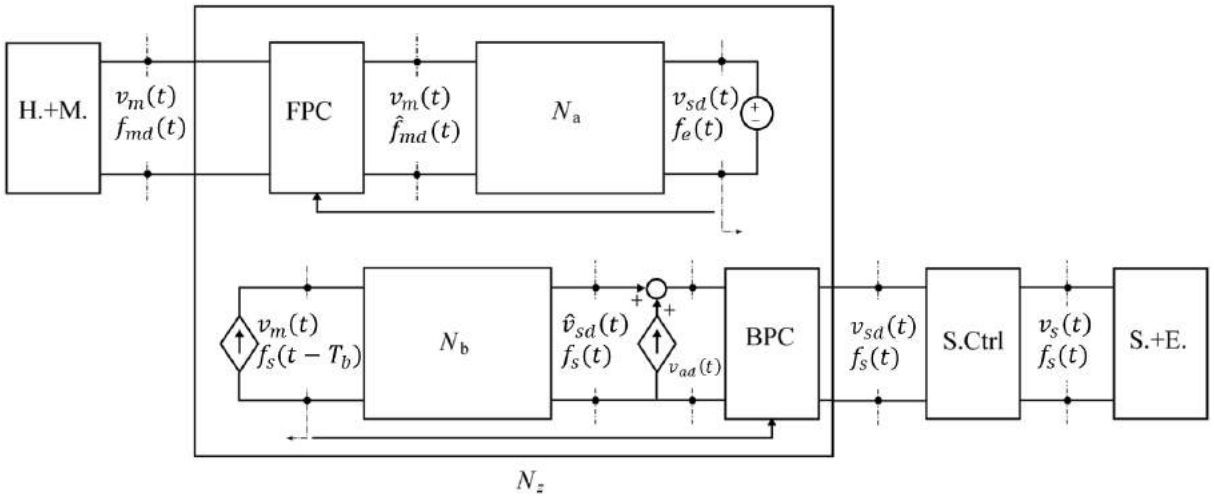

Figure 42: Energy injection via a dependent flow source to compensate for the position drift. Slave PO/PC passivates both the TDPN and the additional flow source.

Figure 43: Master Device: the Arm Light Exoskeleton (ALEx).

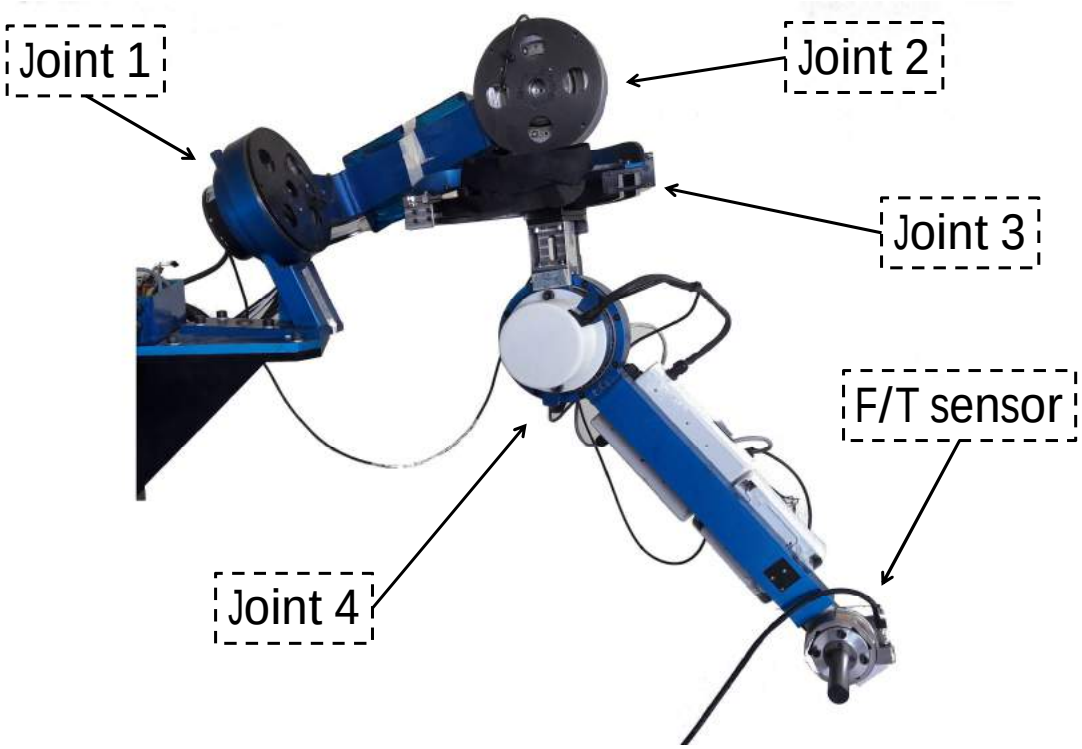

Figure 44: Slave device: the Rehab-Exos exoskeleton

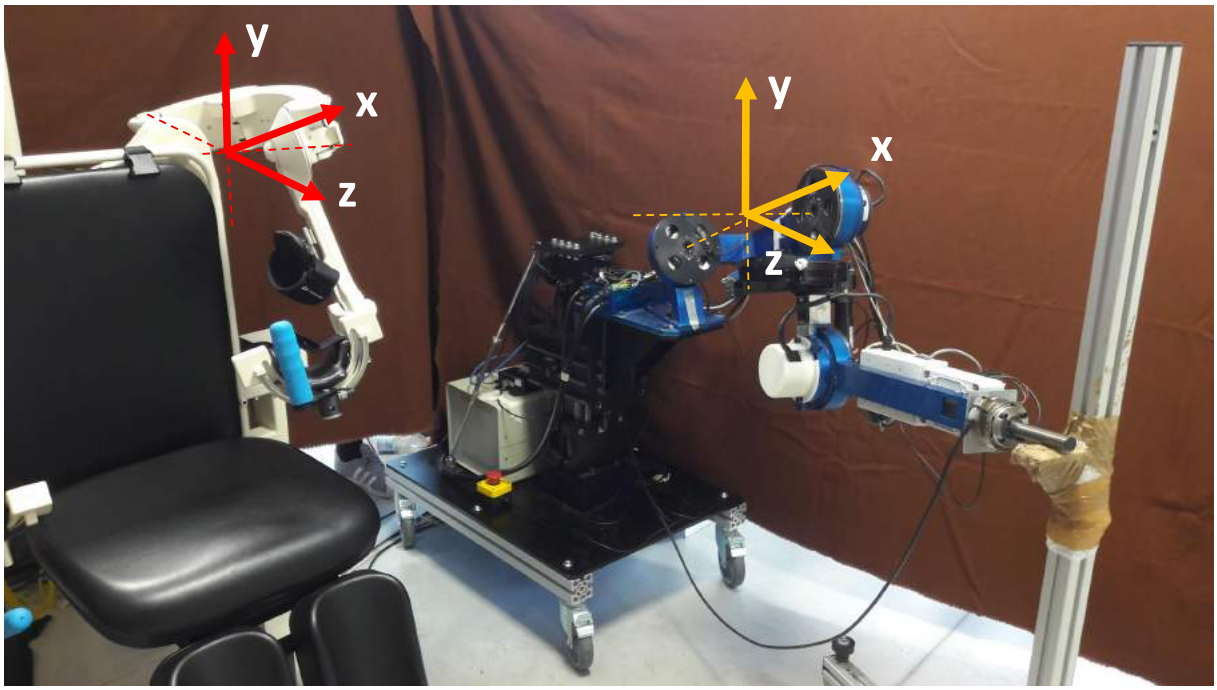

Figure 45: The setup of the experiments with the reference systems of the two robots. On the left, the master device without the human operator. In the center, the slave device. On the right, a physical contact with a rigid environment.

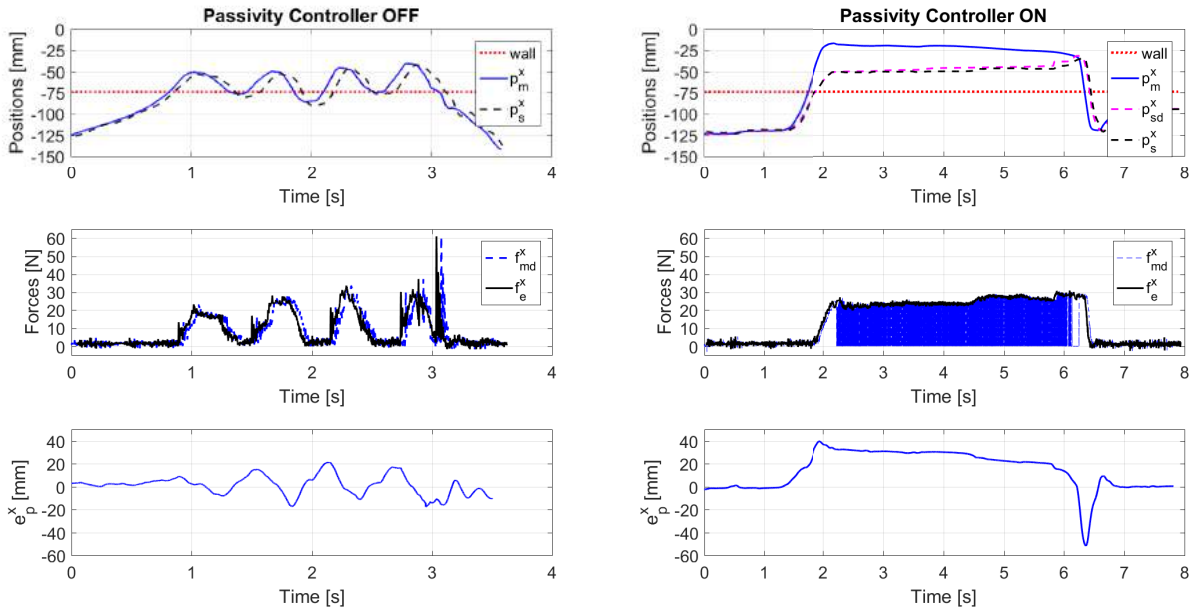

Figure 46: Comparison between a stable and an unstable contact along the X axis. The left part refers to the experiments without the passivity controller, while the right part refers to the experiments with the passivity controller. At the first row the end-effector positions of the master and the slave are reported. The dotted red line is the position of the rigid surface (called wall). The measured master position is in blue solid line. The slave measured positions is in black dashed line, while the slave desired position is in magenta dashed line. At the second row the forces are shown: the blue dashed line is the master desired force while the black solid line is the slave measured force. At the third row the position error between the master measured position and slave measured position is shown.

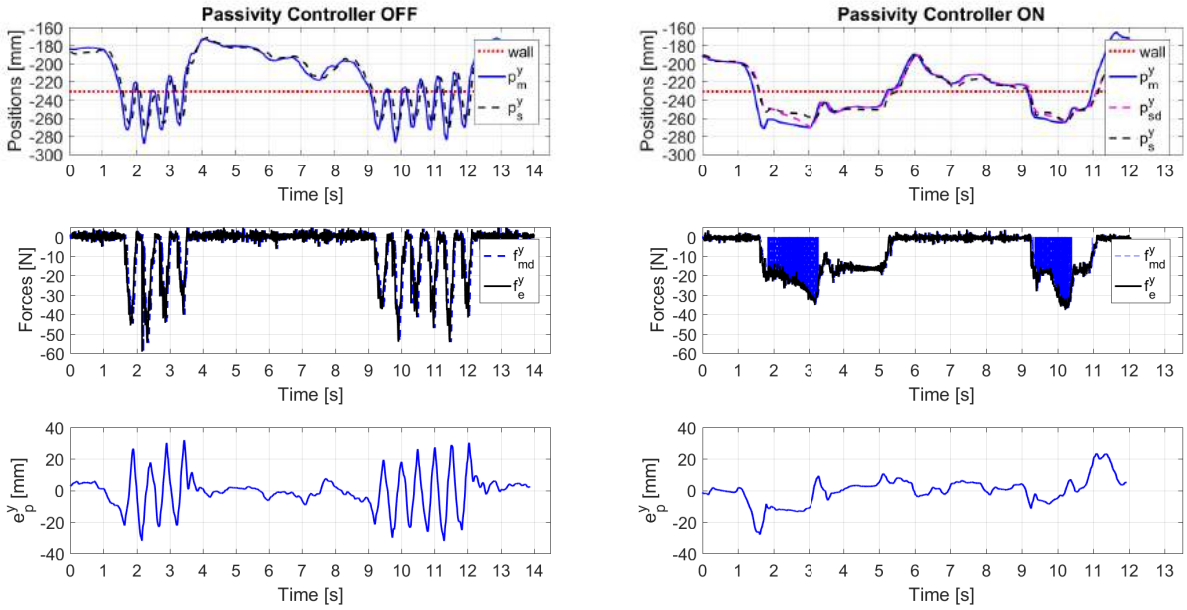

Figure 47: Comparison between a stable and an unstable contact along the Y axis. The left part refers to the experiments without the passivity controller, while the right part refers to the experiments with the passivity controller. At the first row the end-effector positions of the master and the slave are reported. The dotted red line is the position of the rigid surface (called wall). The measured master position is in blue solid line. The slave measured positions is in black dashed line, while the slave desired position is in magenta dashed line. At the second row the forces are shown: the blue dashed line is the master desired force while the black solid line is the slave measured force. At the third row the position error between the master measured position and slave measured position is shown.

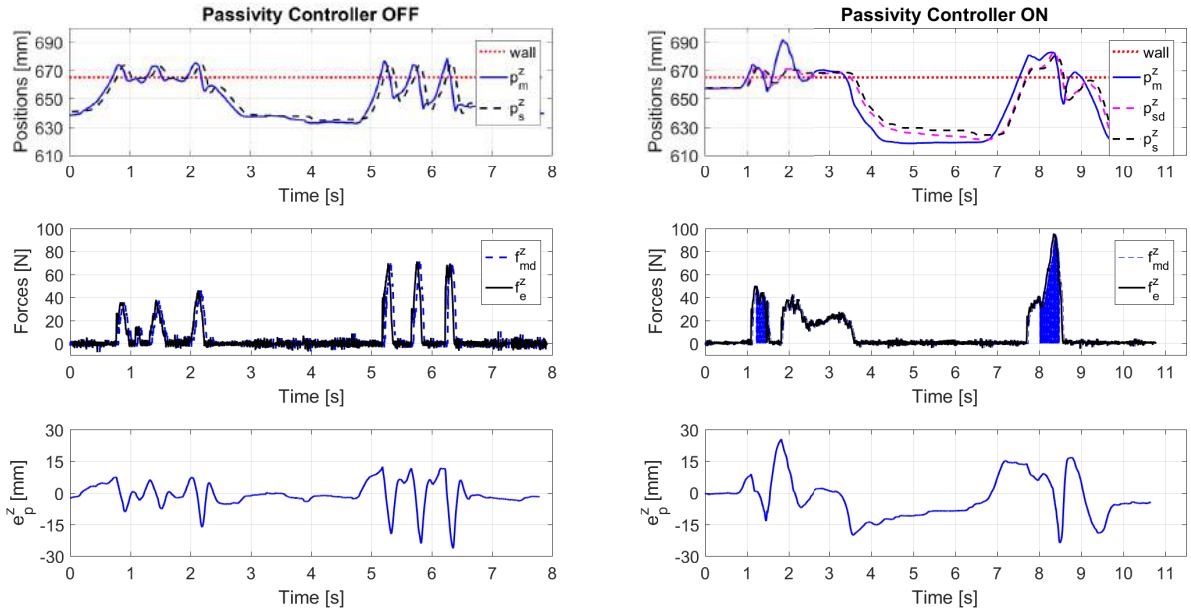

Figure 48: Comparison between a stable and an unstable contact along the Z axis. The left part refers to the experiments without the passivity controller, while the right part refers to the experiments with the passivity controller. At the first row the end-effector positions of the master and the slave are reported. The dotted red line is the position of the rigid surface (called wall). The measured master position is in blue solid line. The slave measured positions is in black dashed line, while the slave desired position is in magenta dashed line. At the second row the forces are shown: the blue dashed line is the master desired force while the black solid line is the slave measured force. At the third row the position error between the master measured position and slave measured position is shown.

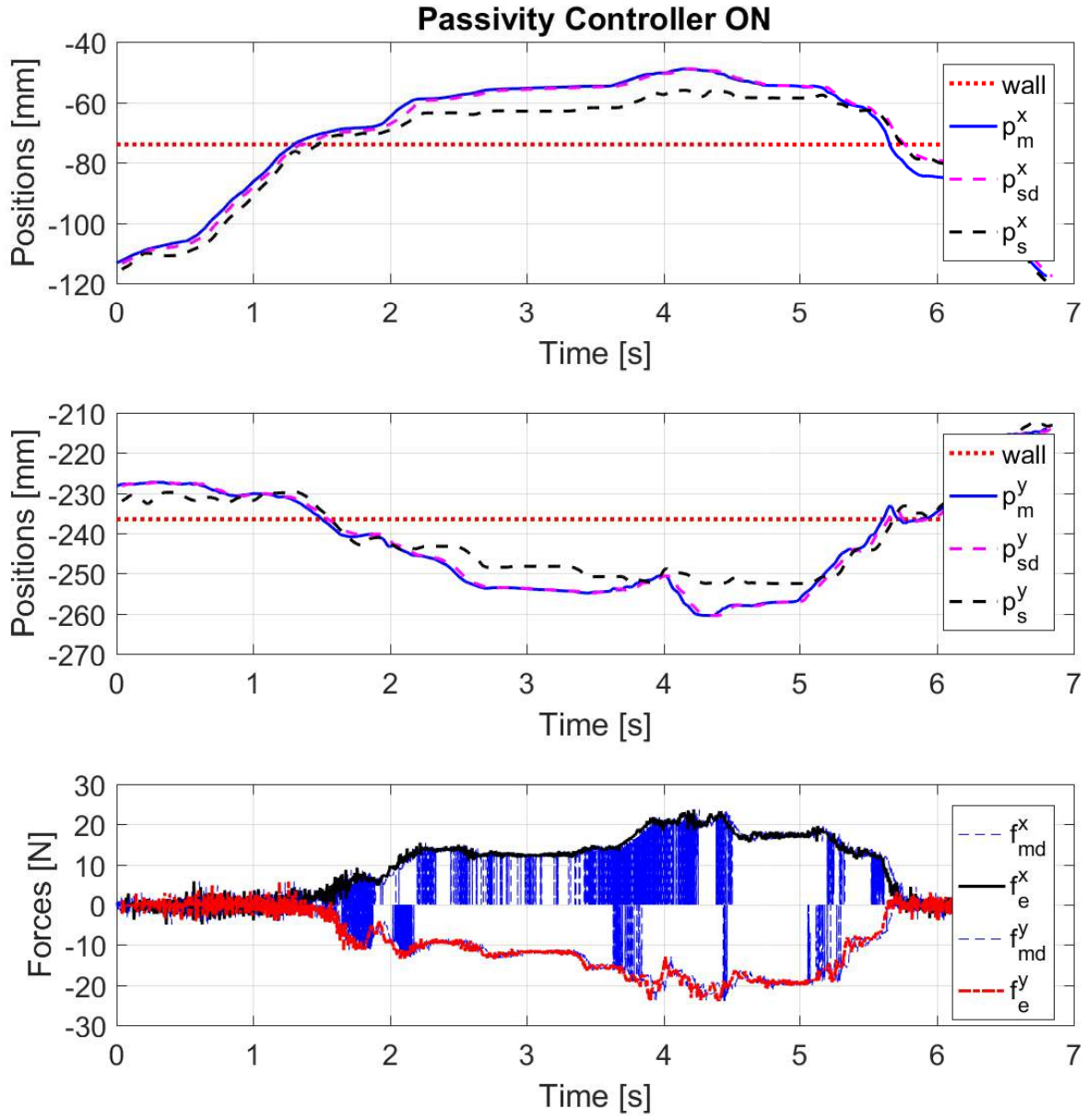

Figure 49: The position and the force profiles along the x and y axes of the master and slave devices during the corner experiment with delayed communication and passivity controller enabled.

8 Workspace Visualization

The color cameras afford the operator with a wide field of view, but only from a single viewpoint. At the same time, the onboard lidar (Velodyne Puck) and RGBD camera respectively generate wide area point-clouds for navigation and short-range high-resolution depth maps for workspace perception. By fusing these disparate sources of video and geometric information, it is possible to reconstruct the robot's current environment as a 3D scene. The operator can then pan, rotate, and zoom in this 3D-mesh representation to gain further understanding of the environment. To this end, we have developed a ROS-node that merges color images with time-of-flight point-clouds and depth maps.

At present, the module first receives point-clouds from the lidar and transforms them into the coordinate system of a virtual depth sensor with a spherical sensor surface, located at the mean position of the color cameras. The points are subsequently projected (or "splatted") onto the virtual sensor sphere, forming a surround-view depth map. The 3D coordinates of the spherical sensor are then projected into each of the cameras' image planes, establishing correspondences between the depth map and camera pixels. The depth map is then easily converted into a 3D mesh. Using the known depth-map to pixel correspondences, we then texture the mesh with the color images that are simultaneously received by the node. The result is a textured mesh that the operator can view from any angle. An example visualization can be seen in figure 50.

Figure 50: Example visualization of a textured mesh generated from a synthetic scene for two different points of view.

The creation of the mesh and texture from the point-cloud data and the image data is integrated into a ROS node. The messages used to communicate with this node are specified as follows:

TextureMesherInput.msg [input]

```
# Message containing input data for creating textured mesh

# Header specifying coordinate frame of point-cloud and time-stamp for recorded point-cloud
std_msgs/Header header

# Point-cloud used for creating mesh
sensor_msgs/PointCloud2 cloud

# Vector filled with images which are used to texture the mesh
sensor_msgs/Image[] images

# Camera info containing the extrinsic and intrinsic calibration of each camera relative to the
coordinate system of the point-cloud
sensor_msgs/CameraInfo[] camInfos
```

TexturedPolygonMesh.msg [output]

```
# Message containing the output data structure with the textured mesh

# Header specifying coordinate frame of texture and time-stamp
std_msgs/Header header

# Point-cloud containing the 3D position of each vertex sensor_msgs/PointCloud2 cloud

# A vector of vertex indices for each sub-mesh
csplat_interface/SubMeshVerts[] vertices

# A vector of texture coordinates for each sub-mesh, one per coordinate
csplat_interface/SubMeshTexCoords[] uTexCoords
csplat_interface/SubMeshTexCoords[] vTexCoords
```

SubMeshVerts.msg [extra]

```
# Message containing the vertices of a sub-mesh
csplat_interface/Polygons[] faces
```

Polygons.msg [extra]

```
# Message containing the vertices creating a polygon (triangles or quads mostly)
csplat_interface/uint32[] faceVerts
```

SubMeshTexCoords.msg [extra]

```
# Message containing one of the texture coordinates of a sub-mesh
csplat_interface/Polygons[] faces
```

The *TexturedPolygonMesh* message follows the structure of *PCL::TexturedMesh*. This class separates the mesh into sub-meshes depending on the texture that its texture coordinates refers to. As such, it contains a point-cloud, with the position of each vertex, and a header specifying the time of data collection as well as information about the coordinate system. The message contains also a number of sub-meshes, equal to the number of cameras + 1. The extra sub-mesh is created from the leftover parts of the mesh, where there are no color information from any camera. Each sub-mesh contains vertex indices describing to how the points in the cloud are connected, as well as the texture coordinates.

The input data contains a point-cloud, collected from lidar, RGBD sensors or other sources, as well as a set of images used for mesh texturing. The *TextureMesherInput* message contains also internal and external calibration parameters for each camera.

References

[1] M. Aiple and A. Schiele. Pushing the limits of the cybergrasp for haptic rendering. In *2013 IEEE International Conference on Robotics and Automation*, pages 3541–3546, 2013.

[2] Junya Aizawa, Tadashi Masuda, Kashitaro Hyodo, Tetsuya Jinno, Kazuyoshi Yagishita, Koji Nakamaru, Takayuki Koyama, and Sadao Morita. Ranges of active joint motion for the shoulder, elbow, and wrist in healthy adults. *Disability and Rehabilitation*, 35(16):1342–1349, 2013. PMID: 23826904.

[3] Jordi Artigas, Jee-Hwan Ryu, Carsten Preusche, and Gerd Hirzinger. Network representation and passivity of delayed teleoperation systems. In *Intelligent Robots and Systems (IROS), 2011 IEEE/RSJ International Conference on*, pages 177–183. IEEE, 2011.

[4] P. Ben-Tzvi and Z. Ma. Sensing and force-feedback exoskeleton (safe) robotic glove. *IEEE Transactions on Neural Systems and Rehabilitation Engineering*, 23(6):992–1002, 2015.

[5] M. Bergamasco, C. A. Avizzano, A. Frisoli, E. Ruffaldi, and S. Marcheschi. Design and validation of a complete haptic system for manipulative tasks. *Advanced Robotics*, 20(3):367–389, 2006.

[6] Massimo Bergamasco, Antonio Frisoli, and Carlo Alberto Avizzano. *Exoskeletons as Man-Machine Interface Systems for Teleoperation and Interaction in Virtual Environments*, pages 61–76. Springer Berlin Heidelberg, Berlin, Heidelberg, 2007.

[7] TMW Burton, R Vaidyanathan, SC Burgess, AJ Turton, and C Melhuish. Development of a parametric kinematic model of the human hand and a novel robotic exoskeleton. In *Rehabilitation robotics (ICORR), 2011 IEEE international conference on*, pages 1–7. IEEE, 2011.

[8] Leonardo Cappello, Naveen Elangovan, Sara Contu, Sanaz Khosravani, Jrgen Konczak, and Lorenzo Masia. Robot-aided assessment of wrist proprioception. *Frontiers in Human Neuroscience*, 9:198, 2015.

[9] Marco Cempini, Mario Cortese, and Nicola Vitiello. A powered finger–thumb wearable hand exoskeleton with self-aligning joint axes. *IEEE/ASME Transactions on Mechatronics*, 20(2):705–716, 2015.

[10] P Cerveri, E De Momi, M Marchente, N Lopomo, G Baud-Bovy, RML Barros, and G Ferrigno. In vivo validation of a realistic kinematic model for the trapezio-metacarpal joint using an optoelectronic system. *Annals of biomedical engineering*, 36(7):1268–1280, 2008.

[11] Lillian Y Chang and Nancy S Pollard. Method for determining kinematic parameters of the in vivo thumb carpometacarpal joint. *IEEE Transactions on Biomedical Engineering*, 55(7):1897–1906, 2008.

[12] A. Chiri, N. Vitiello, F. Giovacchini, S. Roccella, F. Vecchi, and M.C. Carrozza. Mechatronic design and characterization of the index finger module of a hand exoskeleton for post-stroke rehabilitation. *IEEE/ASME Transactions on Mechatronics*, 17(5):884–894, 2012.

[13] Ismail Hakan Ertas, Elif Hocaoglu, and Volkan Patoglu. AssistOn-Finger: An underactuated finger exoskeleton for robot-assisted tendon therapy. *Robotica*, 2014.

[14] M. Fontana, A. Dettori, F. Salsedo, and M. Bergamasco. Mechanical design of a novel hand exoskeleton for accurate force displaying. In *Robotics and Automation, 2009. ICRA '09. IEEE International Conference on*, pages 1704–1709, 2009.

[15] Deanna H. Gates, Lisa Smurr Walters, Jeffrey Cowley, Jason M. Wilken, and Linda Resnik. Range of motion requirements for upper-limb activities of daily living. *Am J Occup Ther*, 70(1):7001350010p1–7001350010p10, Dec 2016. 015487[PII].

[16] DJ Giurintano, AM Hollister, WL Buford, DE Thompson, and LM Myers. A virtual five-link model of the thumb. *Medical engineering & physics*, 17(4):297–303, 1995.

[17] R. A. R. C. Gopura and K. Kiguchi. Development of an exoskeleton robot for human wrist and forearm motion assist. In *2007 International Conference on Industrial and Information Systems*, pages 535–540, Aug 2007.

[18] Florian Gosselin, T. Jouan, J. Brisset, and C. Andriot. Design of a wearable haptic interface for precise finger interactions in large virtual environments. In *Eurohaptics Conference and Symposium on Haptic Interfaces for Virtual Environment and Teleoperator Systems, World Haptics*, pages 202–207, 2005.

[19] Dr Guilherme N. DeSouza, Patrick Aubin, Kelsey Petersen, Hani Sallum, Conor Walsh, Annette Correia, and Leia Stirling. A pediatric robotic thumb exoskeleton for at-home rehabilitation: The isolated orthosis for thumb actuation (iota). *International Journal of Intelligent Computing and Cybernetics*, 7(3):233–252, 2014.

[20] Abhishek Gupta, Marcia K. O'Malley, Volkan Patoglu, and Charles Burgar. Design, control and performance of ricewrist: A force feedback wrist exoskeleton for rehabilitation and training. *The International Journal of Robotics Research*, 27(2):233–251, 2008.

[21] Osama Halabi and Haruhisa Kawasaki. Five fingers haptic interface robot hiro: Design, rendering, and applications. *Advances in Haptics*, 2010.

[22] Y. Hasegawa, J. Tokita, K. Kamibayashi, and Y. Sankai. Evaluation of fingertip force accuracy in different support conditions of exoskeleton. In *IEEE International Conference on Robotics and Automation (ICRA)*, pages 680–685, 2011.

[23] Pilwon Heo, Gwang Min Gu, Soo-jin Lee, Kyehan Rhee, and Jung Kim. Current hand exoskeleton technologies for rehabilitation and assistive engineering. *International Journal of Precision Engineering and Manufacturing*, 13(5):807–824, 2012.

[24] J. Iqbal, N.G. Tsagarakis, and D.G. Caldwell. A multi-DoF robotic exoskeleton interface for hand motion assistance. In *IEEE International Conference of the Engineering in Medicine and Biology Society*, pages 1575–1578, 2011.

[25] Bongsu Kim and Ashish D Deshpande. An upper-body rehabilitation exoskeleton harmony with an anatomical shoulder mechanism: Design, modeling, control, and performance evaluation. *The International Journal of Robotics Research*, page 0278364917706743, 2017.

[26] HI Krebs, N Hogan, W Durfee, and H Herr. Rehabilitation robotics, orthotics, and prosthetics. *Textbook of Neural Repair and Rehabilitation*, 2:165–181, 2006.

[27] T. Laliberte, L. Birglen, and C. Gosselin. Underactuation in robotic grasping hands. *Machine Intelligence & Robotic Control*, 4(3):1–11, 2002.

[28] Daniele Leonardis, Michele Barsotti, Claudio Loconsole, Massimiliano Solazzi, Marco Troncossi, Claudio Mazzotti, Vincenzo Parenti Castelli, Caterina Procopio, Giuseppe Lamola, Carmelo Chisari, et al. An emg-controlled robotic hand exoskeleton for bilateral rehabilitation. 2015.

[29] Jiting Li, Ruoyin Zheng, Yuru Zhang, and Jianchu Yao. iHandRehab: An interactive hand exoskeleton for active and passive rehabilitation. In *IEEE International Conference on Rehabilitation Robotics (ICORR)*, pages 1 – 6, 2011.

[30] D. Lobo, M. Sarac, M. Verschoor, M. Solazzi, A. Frisoli, and M. A. Otaduy. Proxy-based haptic rendering for underactuated haptic devices. In *IEEE World Haptics Conference (WHC)*, pages 1–6, 2017.

[31] G. R. Luecke. Haptic interactions using virtual manipulator coupling with applications to underactuated systems. *IEEE Transactions on Robotics*, 27(4):730–740, 2011.

[32] Paweł Maciejasz, Jörg Eschweiler, Kurt Gerlach-Hahn, Arne Jansen-Troy, and Steffen Leonhardt. A survey on robotic devices for upper limb rehabilitation. *Journal of neuroengineering and rehabilitation*, 11(1):3, 2014.

[33] J. A. Martinez, P. Ng, S. Lu, M. S. Campagna, and O. Celik. Design of wrist gimbal: A forearm and wrist exoskeleton for stroke rehabilitation. In *2013 IEEE 13th International Conference on Rehabilitation Robotics (ICORR)*, pages 1–6, June 2013.

[34] L. Meli and D. Prattichizzo. *Task-Oriented Approach to Simulate a Grasping Action Through Underactuated Haptic Devices*, pages 249–257. Springer Berlin Heidelberg, Berlin, Heidelberg, 2014.

[35] Tobias Nef, Marco Guidali, and Robert Riener. Armin iii–arm therapy exoskeleton with an ergonomic shoulder actuation. *Applied Bionics and Biomechanics*, 6(2):127–142, 2009.

[36] A. U. Pehlivan, S. Lee, and M. K. O'Malley. Mechanical design of ricewrist-s: A forearm-wrist exoskeleton for stroke and spinal cord injury rehabilitation. In *2012 4th IEEE RAS EMBS International Conference on Biomedical Robotics and Biomechatronics (BioRob)*, pages 1573–1578, Rome, Italy, June 2012.

[37] Ali Utku Pehlivan, Fabrizio Sergi, Andrew Erwin, Nuray Yozbatiran, Gerard E. Francisco, and Marcia K. O'Malley. Design and validation of the ricewrist-s exoskeleton for robotic rehabilitation after incomplete spinal cord injury. *Robotica*, 32(8):14151431, 2014.

[38] Joel C Perry, Jacob Rosen, and Stephen Burns. Upper-limb powered exoskeleton design. *IEEE/ASME transactions on mechatronics*, 12(4):408–417, 2007.

[39] E. Pezent, C. G. Rose, A. D. Deshpande, and M. K. O'Malley. Design and characterization of the openwrist: A robotic wrist exoskeleton for coordinated hand-wrist rehabilitation. In *2017 International Conference on Rehabilitation Robotics (ICORR)*, pages 720–725, July 2017.

[40] Elvira Pirondini, Martina Coscia, Simone Marcheschi, Gianluca Roas, Fabio Salsedo, Antonio Frisoli, Massimo Bergamasco, and Silvestro Micera. *Evaluation of a New Exoskeleton for Upper Limb Post-stroke Neuro-rehabilitation: Preliminary Results*, pages 637–645. Springer International Publishing, Cham, 2014.

[41] Elvira Pirondini, Martina Coscia, Simone Marcheschi, Gianluca Roas, Fabio Salsedo, Antonio Frisoli, Massimo Bergamasco, and Silvestro Micera. Evaluation of the effects of the arm light exoskeleton on movement execution and muscle activities: a pilot study on healthy subjects. *Journal of neuroengineering and rehabilitation*, 13(1):9, 2016.

[42] Dongseok Ryu, Kyung-Won Moon, Hyungdo Nam, Yongkwun Lee, Changmook Chun, Sungchul Kang, and Jea-Bok Song. Micro hydraulic system using slim artificial muscles for a wearable haptic glove. In *2008 IEEE/RSJ International Conference on Intelligent Robots and Systems*, pages 3028–3033, 2008.

[43] Jaiyoung Ryu, William P. Cooney, Linda J. Askew, Kai-Nan An, and Edmund Y.S. Chao. Functional ranges of motion of the wrist joint. *The Journal of Hand Surgery*, 16(3):409 – 419, 1991.

[44] Veronica J Santos and Francisco J Valero-Cuevas. Reported anatomical variability naturally leads to multimodal distributions of denavit-hartenberg parameters for the human thumb. *IEEE Transactions on Biomedical Engineering*, 53(2):155–163, 2006.

[45] Mine Sarac, Massimiliano Solazzi, Daniele Leonardis, Edoardo Sotgiu, Massimo Bergamasco, and Antonio Frisoli. *Design of an Underactuated Hand Exoskeleton with Joint Estimation*, pages 97–105. Springer International Publishing, 2017.

[46] Mine Sarac, Massimiliano Solazzi, Daniele Leonardis, Edoardo Sotgiu, Massimo Bergamasco, and Antonio Frisoli. *Design of an Underactuated Hand Exoskeleton with Joint Estimation*, pages 97–105. Springer International Publishing, Cham, 2017.

[47] Mine Sarac, Massimiliano Solazzi, Edoardo Sotgiu, Massimo Bergamasco, and Antonio Frisoli. Design and kinematic optimization of a novel underactuated robotic hand exoskeleton. *Meccanica*, pages 1–13, 2016.

[48] A. Schiele and F. C. T. van der Helm. Kinematic design to improve ergonomics in human machine interaction. *IEEE Transactions on Neural Systems and Rehabilitation Engineering*, 14(4):456–469, Dec 2006.

[49] W Paul Smutz, Apichai Kongsayreepong, Richard E Hughes, Glen Niebur, William P Cooney, and Kai-Nan An. Mechanical advantage of the thumb muscles. *Journal of biomechanics*, 31(6):565–570, 1998.

[50] Panagiotis Stergiopoulos, Guillaume Moreau, Mehdi Ammi, and Philippe Fuchs. A framework for the haptic rendering of the human hand. In *Haptic Interfaces for Virtual Environment and Teleoperator Systems, 2003. HAPTICS 2003. Proceedings. 11th Symposium on*, pages 340–347. IEEE, 2003.

[51] C. S. Tzafestas. Whole-hand kinesthetic feedback and haptic perception in dextrous virtual manipulation. *IEEE Transactions on Systems, Man, and Cybernetics - Part A: Systems and Humans*, 33(1):100–113, 2003.

[52] Furui Wang, Christopher L Jones, Milind Shastri, Kai Qian, Derek G Kamper, and Nilanjan Sarkar. Design and evaluation of an actuated exoskeleton for examining motor control in stroke thumb. *Advanced Robotics*, 30(3):165–177, 2016.

[53] Youngil Youm and Adrian E Flatt. Design of a total wrist prosthesis. *Annals of biomedical engineering*, 12(3):247–262, 1984.